Measurement of the $t\bar{t}$ Production Cross Section at $\sqrt{s} = 1.96$ TeV in the $e+$ jets Final State of $p\bar{p}$ Collisions at the Tevatron

by

DooKee Cho

Submitted in Partial Fulfillment

of the

Requirements for the Degree

Doctor of Philosophy

Supervised by

Professor Thomas Ferbel

Department of Physics and Astronomy

The College

Arts and Sciences

University of Rochester

Rochester, New York

2005

I would like to dedicate this work to my parents and wife.

Curriculum Vitae.

The author was born in Seoul, Korea on October 10, 1968. He attended Korea University from 1988 to 1992, majoring in physics, and graduated with a Bachelor of Arts degree in 1992. He continued to take graduate courses in Particle Physics from 1992 to 1994, and received a Master of Science degree from Korea University in 1994. After he finished his master degree, he did his Military service for two years, and then came to the University of Rochester in the summer of 1997 to begin graduate studies in physics under the direction of Professor Tom Ferbel. In 1998, the author moved to Fermi National Accelerator Laboratory and joined the University of Rochester Group at the DØ Experiment. He received a Master of Arts degree from University of Rochester in 2000, based on a study of position resolution in electron and photon showers in the DØ Calorimeter. His Ph.D research involves the measurement of the $t\bar{t}$ production cross section in $p\bar{p}$ collisions in Run II of the Tevatron. This was performed under the direction of Professor Thomas Ferbel and supervised at Fermilab by Dr. Qizhong Li.

Acknowledgments

I feel fortunate in having worked with my adviser Professor Tom Ferbel. He gave me not only good guidance but also endless support during my entire graduate career. I believe that without this support, I would not have finished my work. I thank him for everything.

I greatly value my association with Dr. Qizhong Li. She has been my mentor since 2001 and has guided me through many pitfalls of my analysis. I owe her a lot for her patience and support during my graduate career. I greatly appreciate her contributions to my development.

I also greatly appreciate my colleagues in the Rochester group at DØ for their support during my studies in this large experiment. I have especially enjoyed working with Marek Zieliński on development of detector software. Also, his advice helped me a lot in various aspects of my work. I was also happy to work with George Ginther, Vishnu Zutshi and Volker Buescher. They gave me a chance to learn much about detector hardware and software.

In developing this analysis, I have received much help from all members of DØ. Especially, I thank Professor Regina Demina, Marc-Andre Pleier, and Michael Begel for many useful discussions. They pointed me to the problems in my analysis, and helped me improve it.

I wish to thank my colleagues Jaedong Lee (Ph.D student at University of

Rochester), Jiyeon Han (Ph.D student at University of Rochester) and Dr. Suyong Choi for useful discussions. Their experience helped me to finish my work successfully. Also, I appreciate Dr. Unki Yang (former Ph.D student in University of Rochester) and Dr. Yonsei Chung for their kind support in helping me settle in the area when I moved to Fermilab in 1998.

I am also appreciative of the great help I have received during my graduate career at the University of Rochester, and especially from the physics department and Barbara Warren.

I must further acknowledge the United States Department of Energy for their support of the DØ experiment.

Last but not least, I am thankful to my parents for their endless support. Also I acknowledge the sacrifice that my wife and son had to make in letting me work on this analysis.

Abstract.

We discuss the measurement of the cross section for $t\bar{t}$ production in $p\overline{p}$ collisions at $\sqrt{s} = 1.96$ TeV in e+jets final states observed at the DØ experiment at the Fermilab Tevatron. Our result is based on data collected from the June 2002 to September 2003 period of Run II of the $p\overline{p}$ Collider.

In the Standard Model, the top quark is expected to decay mainly into a W boson and a b quark. The W boson can decay subsequently into a lepton and its neutrino or a $q'\overline{q}$ quark-antiquark pair. In this thesis, we focus on the $e^+\nu_e$ or $e^-\overline{\nu_e}$ decays of one of the W bosons and the $q'\overline{q}$ decays of the other W boson in $t\bar{t}$ final states. The b, q and q' quarks appear as jets of particles in the detector, thereby defining the e+jets final state. We present two methods used for performing this measurement. The first method is based on a Random Grid Search (RGS) that minimizes the uncertainty on the extracted cross section. The variables used in the search take advantage of differences between expected background and signal processes to obtain the yield of $t\bar{t}$ events. The second method uses a Neural Network (NN) procedure that discriminates signal from background through the application of a NN trained on simulated $t\bar{t}$ signal and W+jets background events.

The preliminary results presented in this thesis for inclusive $t\bar{t}$ production are $\sigma_{p\overline{p}\rightarrow t\bar{t}+X}$ of $7.9^{+2.6}_{-2.4}$ (stat) ${}^{+2.2}_{-2.3}$ (syst) $\pm$ 0.5 ($\mathcal{L}$) pb from the RGS analysis, and $8.1^{+3.1}_{-3.1}$ (stat) ${}^{+1.8}_{-1.3}$ (syst) $\pm$ 0.5 ($\mathcal{L}$) pb for the NN analysis, where the uncertainties correspond to contributions from statistical and systematic sources and from the uncertainty on luminosity. Our measurements are consistent with each other, and are within error of the value of 6.77 ± 0.42 pb expected in the Standard Model.

Contents

List of Figures

List of Tables

Chapter 1

Introduction

The top quark was observed by CDF and DØ collaborations in the spring of 1995 of Run I of the Tevatron collider at Fermilab [1] [2]. Since this discovery, the CDF and DØ collaborations have obtained better precision for measurements of the top-quark mass [3] and the $t\bar{t}$ production cross section [4]. With more data, detailed studies have been refined using better particle-identification techniques and more innovative analysis methods.

To prepare for the even higher luminosity of Run II, the CDF and DØ collaborations have upgraded major components of their detectors, and developed analysis techniques to enhance signal at higher luminosity. The analysis presented in this thesis corresponds to one of the first attempts to extract the cross section for top-quark production in $p\bar{p}$ collisions at a center-of-mass energy $\sqrt{s} = 1.96$ TeV.

The data in this measurement correspond to the e+jets channel of $t\bar{t}$ production.

1.1 The Top Quark in the Standard Model

Quarks and leptons comprise the basic fundamental particles of the Standard Model (SM), and there are six kinds or "flavors" of quarks and leptons, with quite different masses. These quarks and leptons are grouped in pairs into the three generations shown in Fig. 1.1. They, along with their antiparticles, interact through the exchange of spin –1 gauge bosons: eight massless gluons, the massless photon, and the massive $W^{\pm}$ and Z^0 bosons. The SM is extraordinarily successful in that it accommodates all observations and phenomena examined in high energy collisions [5].

$$\begin{array}{llll} \text{Quarks:} & \begin{pmatrix} u \\ d \end{pmatrix} & \begin{pmatrix} c \\ s \end{pmatrix} & \begin{pmatrix} t \\ b \end{pmatrix} \\ \text{Leptons:} & \begin{pmatrix} \nu_e \\ e^- \end{pmatrix} & \begin{pmatrix} \nu_\mu \\ \mu^- \end{pmatrix} & \begin{pmatrix} \nu_\tau \\ \tau^- \end{pmatrix} \end{array}$$

Figure 1.1: The three generations of quarks and leptons in the Standard Model.

The discovery of the tau-lepton (τ) [6], followed by the discovery of Υ at Fermilab [7] in 1977 as a resonance in the $\mu^+\mu^-$ invariant mass spectrum (interpreted as a $b\bar{b}$ bound state) suggested the existence of the top quark, as the third-generation weak-isospin partner of the bottom quark, and the existence of a third-generation quark doublet [8].

The Standard Model predicts the electric charge and weak isospin of the top quark (Q = 2/3, and $I_3 = 1/2$), but its mass remains a free parameter. The most recent value of the top mass is $M_{top} = 178 \pm 4.3$ GeV/c^2 [3].

1.2 Top-Quark Production

At the Tevatron collider, top quark is produced mostly in pairs. The leading-order diagrams shown in Fig. 1.2 of $q\overline{q}$ annihilation and gluon fusion into $t\bar{t}$ provide the major contributions to top production in $p\overline{p}$ collisons.

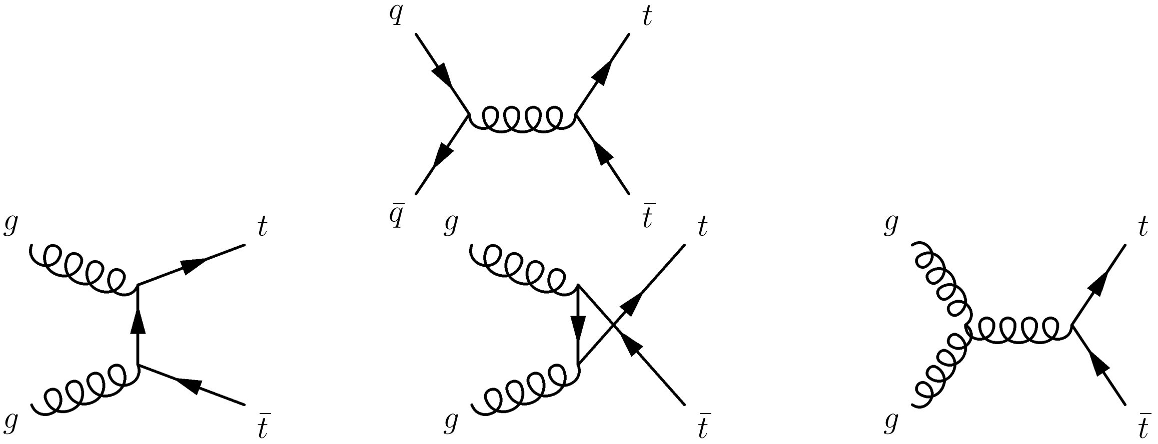

Figure 1.2: Lowest-order Feynman diagrams for production of $t\bar{t}$ pairs in $p\overline{p}$ collisions.

A significant fraction of the energy in a proton and antiproton is carried by a valance quark, and the $q\overline{q}$ channel therefore dominates the $t\bar{t}$ production mechanism. At the Tevatron, the relative contributions of these $q\overline{q} \rightarrow t\overline{t}$ and $gg \rightarrow t\overline{t}$ are about 85% and 15%, respectively [9].

1.3 Top-Quark Decay

The top quark in the SM is expected to decay mainly into a W boson and a b quark. The W boson then decays into a lepton and its neutrino or into a quark and an antiquark ($u\overline{d}$ or $c\overline{s}$ for W^+). The decays of the top quark and of the W are very fast, typically $\lesssim 10^{-24}$ sec [10].

In our study of $t\overline{t}$ production, we focus on the final states where one W decays into $e^+\nu_e$ or $e^-\overline{\nu_e}$, and the other to $q\prime\overline{q}$. The quarks (including the accompanying b quarks) "hadronize" into jets of observable particles [11]. Thus, we examine the final-state topology corresponding to an observed e^+ (or e^-), at least four jets, and a missing (undetected) neutrino.

Chapter 2

Tevatron and the DØ Experiment

The Tevatron collider at the Fermi National Accelerator Laboratory (Fermilab) in Illinois, USA, accelerates both protons and antiprotons to 980 GeV, and provides collisions at a center-of-mass energy of 1.96 TeV. Figure 2.1 shows the Fermilab accelerator chain, described more fully in Section 2.1. DØ is one of the collider experiments at the Tevatron. The DØ detector is designed to study the products of proton and antiproton annihilation, and took its first data in the period 1992-1996 (called Run I) at a center-of-mass energy of 1.8 TeV. This was done using 6×6 proton and antiproton bunches and 3.5 μs intervals between beam crossings, which produced a peak luminosity of the order 10^{31} $\text{cm}^{-2}\text{s}^{-1}$, and collected about 150 pb^{-1} of data. Between 1996 and 2001, the Tevatron was upgraded to obtain a higher center-of-mass energy ($\sqrt{s}$) and luminosity (called Run II). For Run II, the

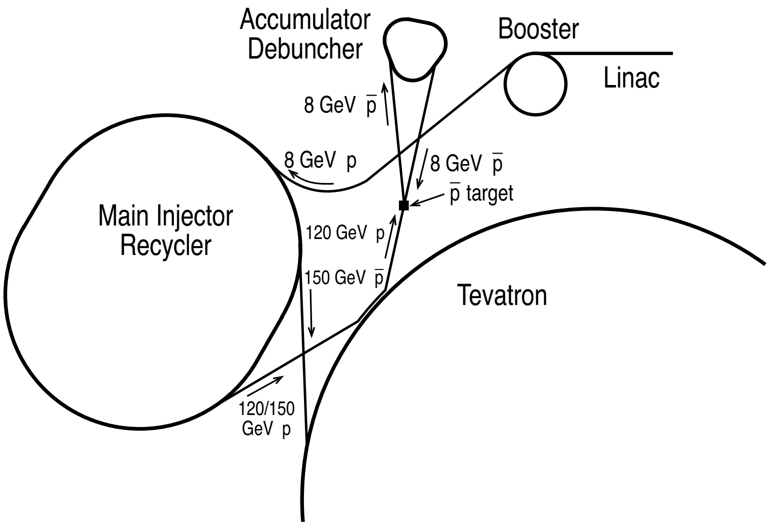

Figure 2.1: The accelerator complex at Fermilab.

center of mass energy was raised to 1.96 TeV, using 36×36 proton and antiproton bunches, and 396 ns between crossings. The peak luminosity reached thus far is $\approx 10^{32}$ cm^{-2}s^{-1}, and the integrated luminosity per week is about 20 pb^{-1}. The expected integrated luminosity for Run II will be 4–8 fb^{-1} [12].

2.1 Accelerator

Run II at Fermilab began in March 2001, and it required major changes to the accelerator complex [13], and to the detectors [14]. The most notable changes include the construction of a new Main Injector [15], which replaced the Main Ring of Run I; the Recycler Ring [15], which is intended to be used for storing antiprotons produced in the $\overline{p}$ source, as well as the antiprotons remaining in the

Tevatron after a store; and an increase in beam energy from 900 GeV to 980 GeV, operating the Tevatron as a 36×36 bunch collider.

The proton source, consists of 25 keV negatively-charged hydrogen ions, that are accelerated to 750 keV in a Cockcroft-Walton accelerator, and bunched and fed into a 150 m long linear accelerator (LINAC), which accelerates the ions to 400 MeV. The ions are then stripped using carbon foils, and the protons are selected and led into the Booster Synchrotron, which raises their energy to 8 GeV [15].

The Main Injector (MI) provides a high repetition rate to support antiproton production, while simultaneously providing more protons for fixed-target operations. It has multiple operating modes, including provision of up to 120 GeV protons for antiproton production, and the acceleration of protons and antiprotons to 150 GeV for injection into the Tevatron [15].

Antiprotons are produced by colliding 120 GeV protons from the Main Injector on a nickel target. Increased antiproton production is a very important factor for Run II, and involves lattice modification of the antiproton target and upgrades in stochastic cooling in the Debuncher and Accumulator to take advantage of the higher repetition rate of the Main Injector [15].

Seven bunches of protons in the Booster are transferred into the Main Injector, accelerated to 150 GeV, coalesced into one bunch, and injected into the Tevatron. The procedure is repeated for 36 bunches, separated by 396 ns, with the bunches routed through the central orbit of the Tevatron. The antiproton beam also consists of sets of 7 bunches from the Accumulator, transferred to the Main Injector and accelerated to 150 GeV. These are coalesced into 4 bunches, and injected into the Tevatron 36 times, and circulate in the Tevatron in a helical orbit separate of the proton beam. The proton and antiproton beams are then accelerated to 980 GeV. Finally, they collide at the interaction regions at BØ and DØ. The collision store lasts for about 24 hours [15].

2.2 DØ Detector

The DØ detector consists of 3 major components: the tracking system, the calorimeter and muon systems (see Fig. 2.2). For Run II, the DØ detector was upgraded in order to take advantage of the anticipated high-luminosity environment [16].

2.2.1 Rapidity and Pseudorapidity

The rapidity y of a particle is defined in terms of a particle's longitudinal momentum (p_z) and energy E, as follows:

$$y = \frac{1}{2} ln \frac{E + p_z}{E - p_z} \tag{2.1}$$

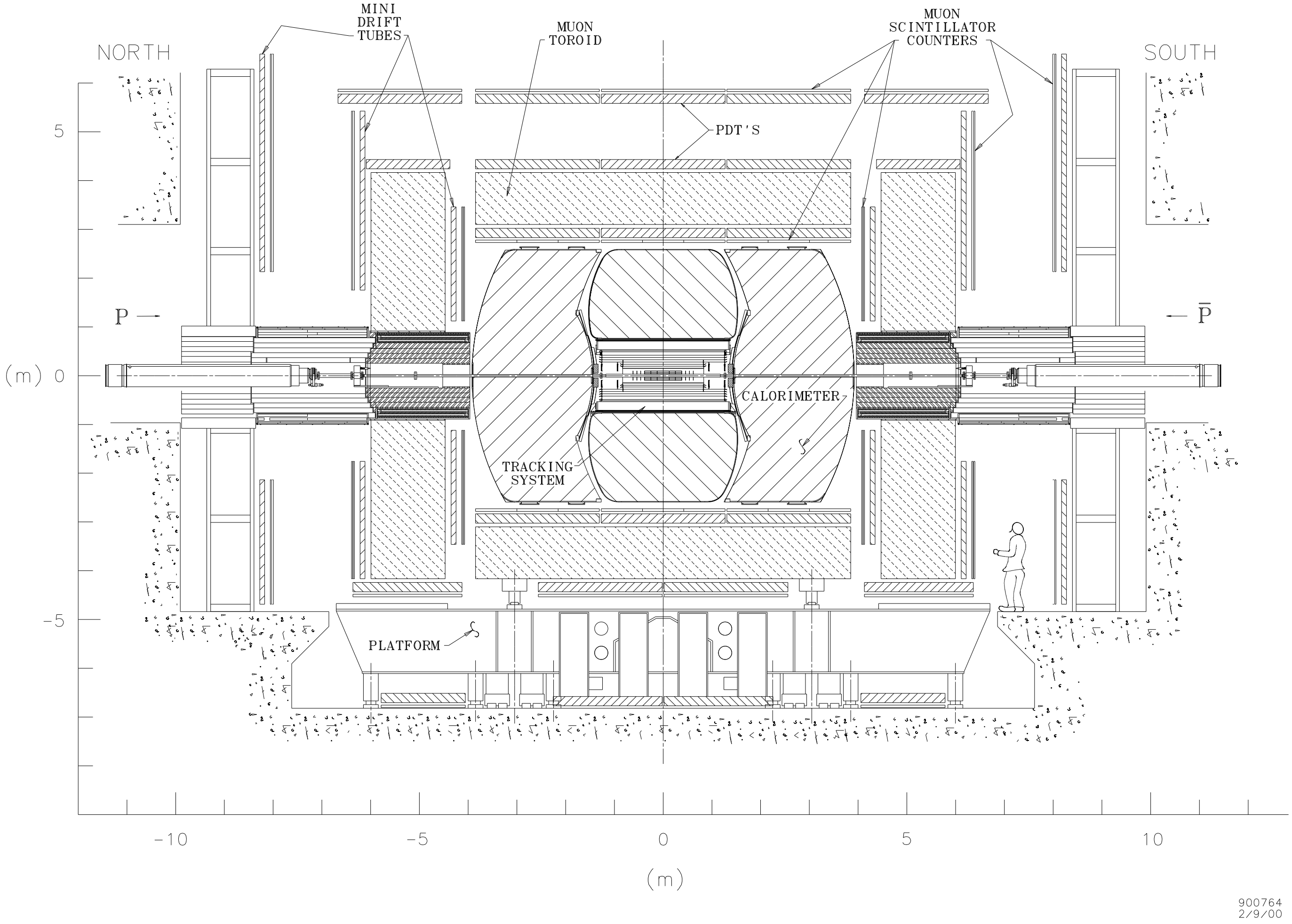

Figure 2.2: Side view of the DØ detector, indicating its major components.

Pseudorapidity (η) is the rapidity, but calculated neglecting the particle's mass, which reduces y to:

$$\eta = -ln\ \tan(\frac{\theta}{2}) \tag{2.2}$$

where θ is the polar angle with respect to the incident proton direction. Zero rapidity (or pseudorapidity) corresponds to particles emitted at 90^o relative to the beamline, and high values of $|y|$ or $|\eta|$ correspond to very forward or backward-going particles. The η variable, when defined relative to the center of the DØ detector provides an excellent way of characterizing the geometry of the system components.

2.2.2 Tracking System

The tracking system (see Fig. 2.3) in the DØ detector consists of an inner Silicon Microstrip Tracker (SMT), surrounded by a Central Scintillating Fiber Tracker (CFT), reside within a 2T superconducting solenoid. Central and forward scintillator Preshower Detectors (CPS and FPS) are located just outside the solenoid. With this upgraded tracking system, DØ can now achieve a momentum measurement through its introduction of a solenoidal field, better electron identification and e/γ discrimination, tracking over a large range of pseudorapidity ($|\eta| < 3$), secondary-vertex measurement for identification of b jets from Higgs bosons and for studies of top and b physics issues, a first-level tracking trigger, fast detector response to enable operation with a bunch-crossing time of 396 ns, and radiation-hard silicon detectors for the high-luminosity Run II [14], [16].

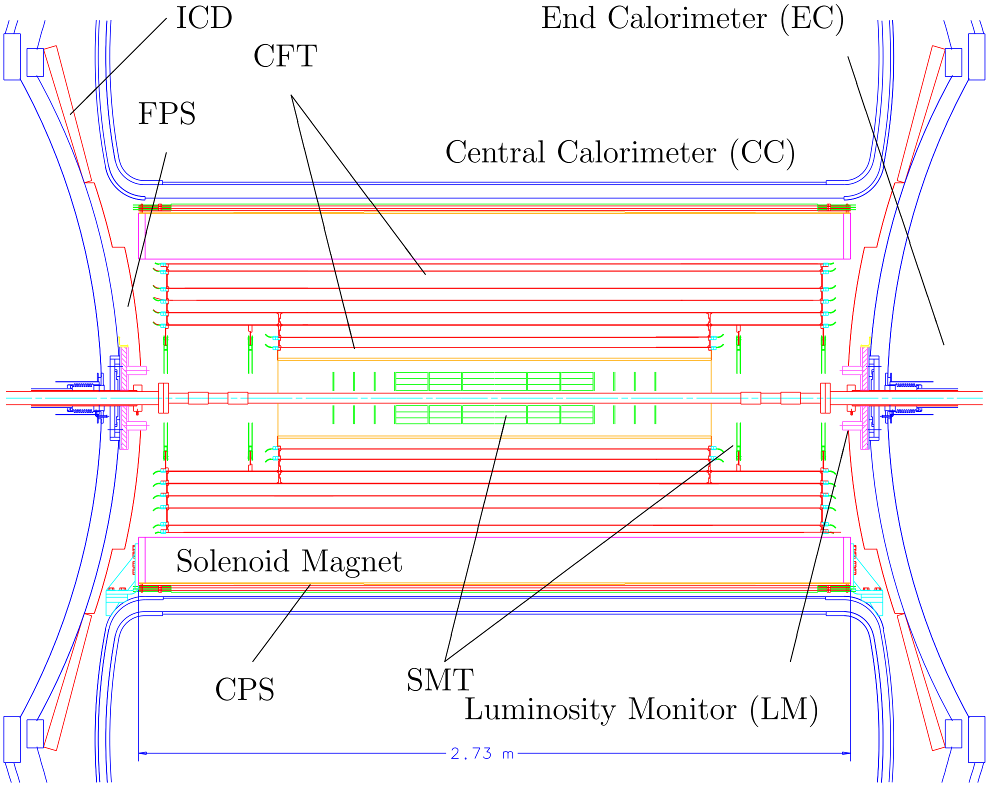

Figure 2.3: Side view of the DØ tracking system.

Silicon Microstrip Tracker (SMT)

The SMT is the detector nearest to the $p\overline{p}$ collision axis at DØ, and provides the high-resolution part of the tracking system [16]. Since collider interactions provide particles at all η, the detector was designed to have a barrel system at central rapidities, measuring primarily the $r-\phi$ coordinate, and disk detectors that provide $r-z$ as well as $r-\phi$ information. The interaction vertices for particles at large $|\eta|$ are reconstructed in three dimensions with help of the disks, and vertices of particles at small $|\eta|$ are determined by the barrels. (The coordinates r, z and ϕ refer to the radial direction, the longitudinal direction, and the azimuth relative to the collision axis, respectfully.)

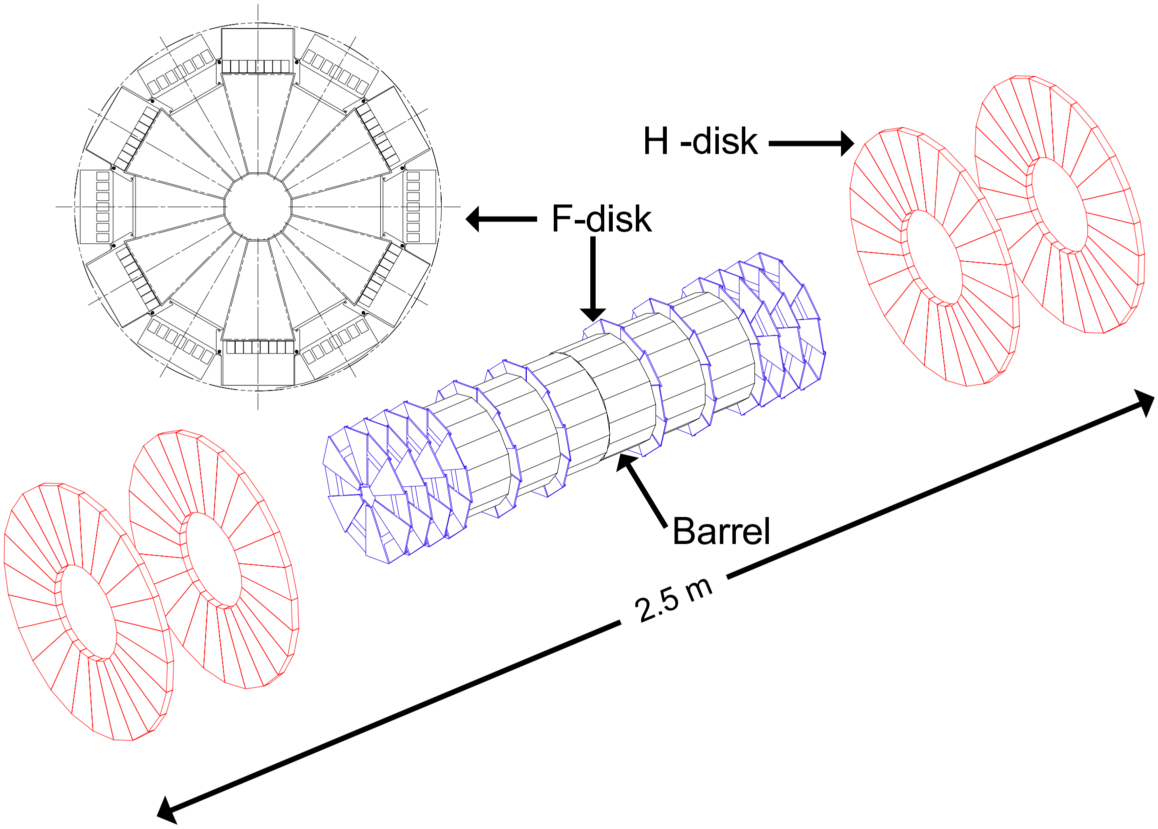

Figure 2.4: Schematic of the Silicon Microstrip Tracker.

Figure 2.4 shows the design of the interspersed disks and barrels. The baseline design has six barrels sections, with the more demanding 90^o double-sided technology detectors used in the central modules. There is a total of ≈ 800,000 channels in the SMT.

Central Fiber Tracker (CFT)

The CFT surrounds the silicon vertex detector, covers the central region of pseudorapidity, and has two main functions. First, with the Silicon Microstrip Tracker, it enables track reconstruction and momentum measurement of all charged particles at $|\eta| < 2.0$, and it also provides fast "Level 1" track triggering for $|\eta| < 1.6$ [16]. Combining information from the tracker with that from the muon and preshower detectors, provides the formation of fast triggers for muons and electrons. These triggers are critical for taking full advantage of the physics opportunities available with the higher luminosities.

The CFT consists of 8 layers, and each layer has a doublet ribbon of axial scintillating fibers and one doublet layer of $\pm 3^0$ stereo fibers [14]. The CFT has a total of about 77,000 channels. The fibers are up to 2.5 m long, and the light is piped out by clear fibers of 7-11 m length to visible light photon counters (VLPC), which are located in a cryostat outside the tracking volume and maintained at 9K. The VLPC is a solid-state device, with pixel size of 1 mm, which is matched to the fiber diameter [14]. The VLPC is an ideal readout for the fiber tracker, because it has a fast reset time, high gain and excellent (≈ 85%) quantum efficiency.

This technology required extensive testing to provide the characterization of the thousands of channels of VLPCs, and a setup of a cosmic ray test stand with fully instrumented fibers [14]. The measured photoelectron yield, a critical measure of system performance, was found to be 8.5 photoelectron per fiber, with 99.5% of the thermal noise below a threshold of one photoelectron [14].

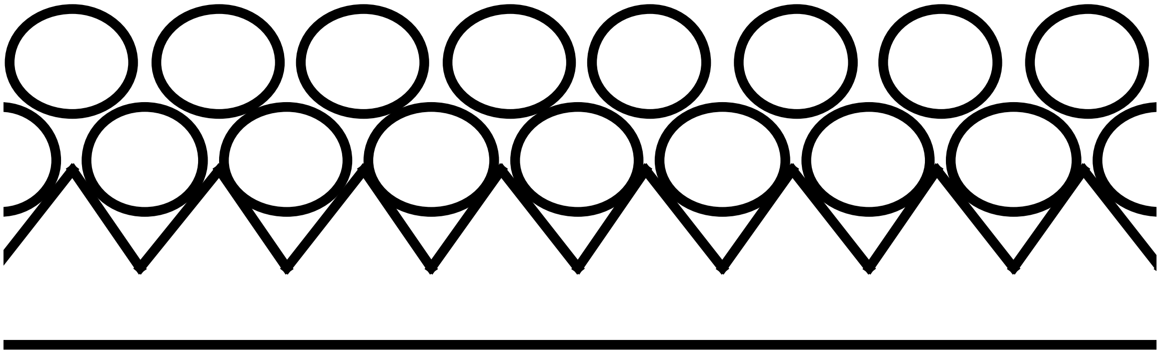

Figure 2.5: The cross section of a segment of a doublet layer in the CFT. The saw-toothed block is a curved connector located at the end of the cylinder.

Superconducting Solenoid

The superconducting solenoid, which is 2.73 m long, and 1.42 m in diameter, provides a 2T magnetic field to measure charged-particle momentum. The superconducting (SC) solenoid, a two-layer coil with mean radius of 60 cm, has a stored energy of 5MJ, and the tracking volume provides a $\sin\theta \times \int B_z dl$ of transverse "kick" along the trajectory of any particle [16].

Preshower detectors

The preshower detectors are designed to help electron identification and triggering by providing precise position information. The central preshower detectors (CPS) are located in the 51 mm gap between the solenoid coil and the central cryostat at a radius of 72 cm, and cover the region of $|\eta| < 1.2$. The CPS consists of triangular scintillator strips with an axial layer and a 20^o stereo layer, both read out using wavelength shifter fibers (WLS). A cross-sectional view of the geometry is given in Fig. 2.6 [16]. With a lead absorber tapered in Z in front of the detector, there are 2 radiation lengths of material, including the solenoid and the lead. The forward preshower detectors (FPS) are located on the inner face of each of the end calorimeter (EC) cryostats and cover $1.4 < |\eta| < 2.5$ of pseudorapidity range.

Use of preshower information with fast-energy and position measurements improves electron purity at the trigger level. The axial layer of the preshower is used in the Level-1 electron trigger, and provides a factor of 3-5 reduction in trigger rate by applying a pulse height requirement and requiring coarse position matching to tracks. In the offline analysis, the early sampling of showers and the good position resolution of the detector provides additional means for identifying electrons, and therefore enhances the capability for tagging of b-quark jets through the decays of B particles within these jets [16].

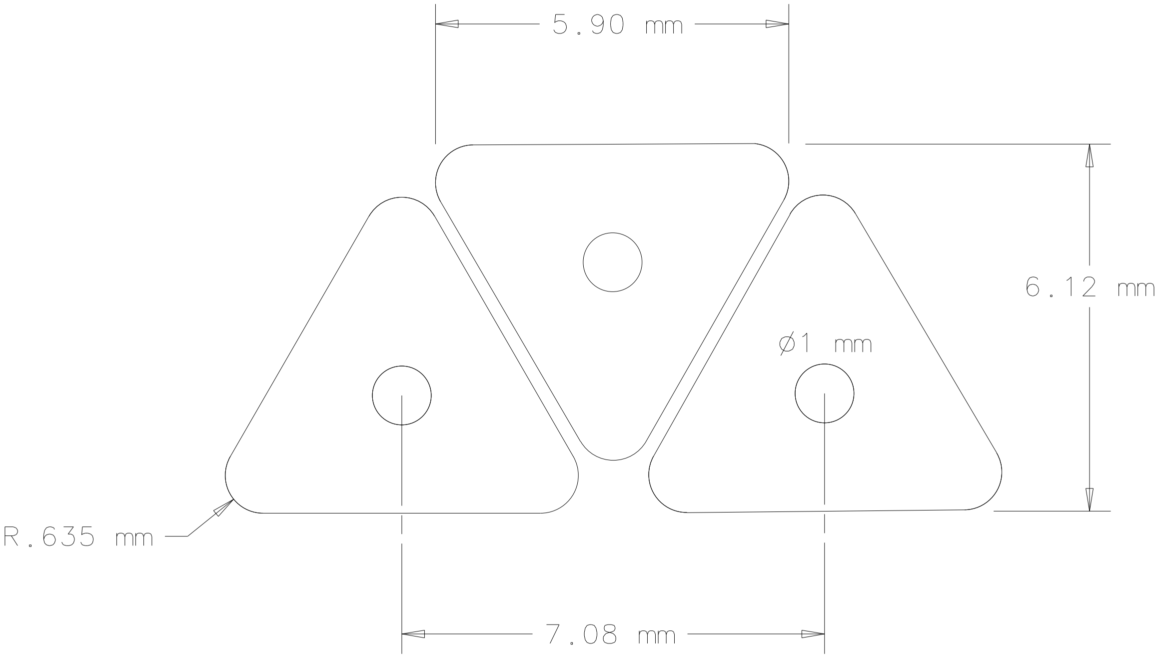

Figure 2.6: The cross section of a layer of the central preshower detector. The triangles are made of extruded plastic scintillator and the circles in the middle of each represent holes that are occupied by wavelength shifting fibers. Each triangular scintillator strip is wrapped in reflective material to increase light yield and reduce cross talk.

2.2.3 Calorimeter

Except for the readout electronics, the DØ calorimeter did not change between Run I and Run II. The DØ calorimeter employs liquid argon as the active medium, which is chosen because of the unit gain that can be achieved with liquid argon, the relative simplicity of calibration, the flexibility offered in segmenting the calorimeter into transverse and longitudinal cells, the good radiation hardness, and the relatively low cost for readout electronics. However, the choice of liquid argon includes the complication of relying on cryogenic systems, the need for a relatively massive containment vessel (cryostat), which implies regions of uninstrumented material, and inaccessibility of modules during operation. A typical cell of the calorimeter is shown in Fig. 2.7.

The calorimeter consists of a central calorimeter (CC), which covers roughly $|\eta| < 1$, and a pair of end calorimeters (EC), which extend the coverage out to $|\eta| \approx 4$ [17]. The boundary between CC and EC was chosen to be approximately perpendicular to the beam direction in order to minimize degradation in the imbalance in transverse momentum (or "missing transverse energy", $\not{E}_T$). The dimensions of the calorimeters were determined by constraints imposed by the size of the experimental hall, the need for adequate depth to ensure good containment of shower energy, the requirements of magnetic measurement of muon momenta outside the calorimeter, and the need for sufficient tracking coverage in front of the calorimetry. The calorimeter has three types of modules in the CC and EC [17]: an electromagnetic section (EM), with relatively thin (several mm) uranium absorber plates, a fine-hadronic section with thicker ($\approx$ 6 mm) uranium plates, and

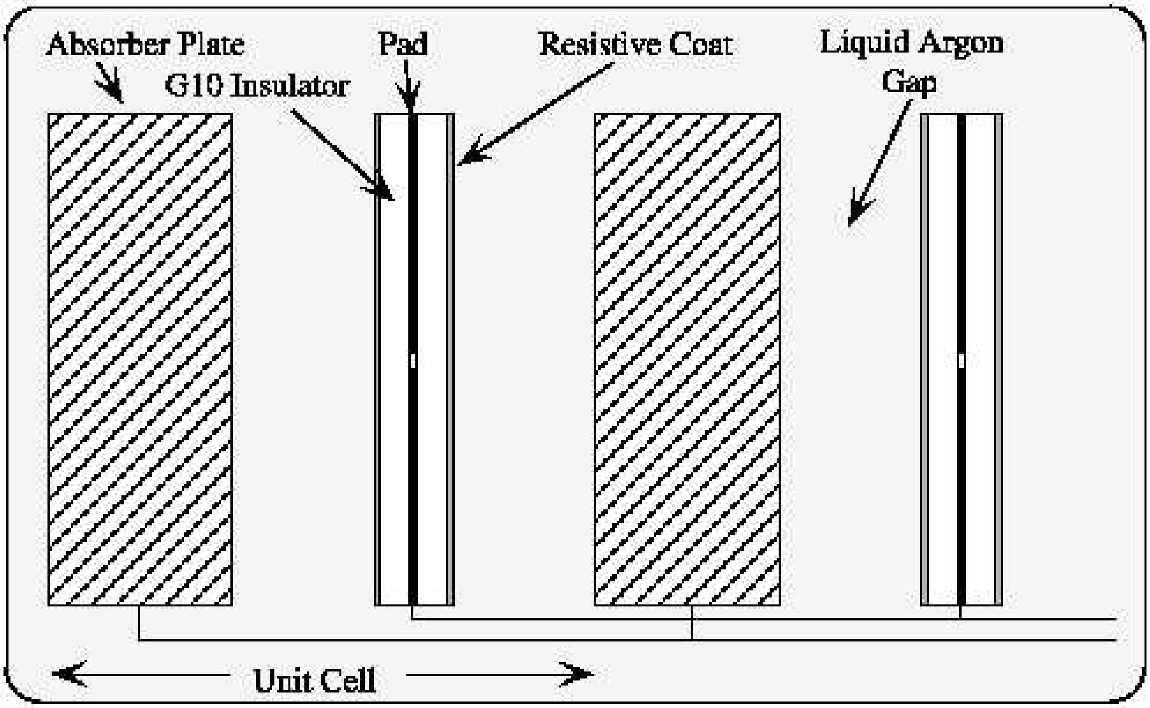

Figure 2.7: Schematic of two calorimeter cells. The resistive coat is kept at high voltage (≈ 2 kV), and the argon gaps provide a drift distance of ≈ 2.3 mm.

a coarse-hadronic section with thick (≈ 5 cm) copper or stainless steel plates. The coarse sections provide sampling of the remnant hadronic showers, while keeping the material density high and outer radius relatively small.

The pattern and sizes of the readout cells (pads) are crucial elements of the calorimeter design. The typical transverse size of EM showers is 1-2 cm, and 10 cm for hadronic showers. We define the variable $\Delta\mathrm{R} = \sqrt{\Delta\eta^2 + \Delta\phi^2}$, where ΔR ≈ 0.5 corresponds to the typical size of parton jets. A fine segmentation of the calorimeter helps probe the shape of showers in each section (EM, fine hadronic and coarse hadronic sections) of the calorimeter, and provides a way to distinguish

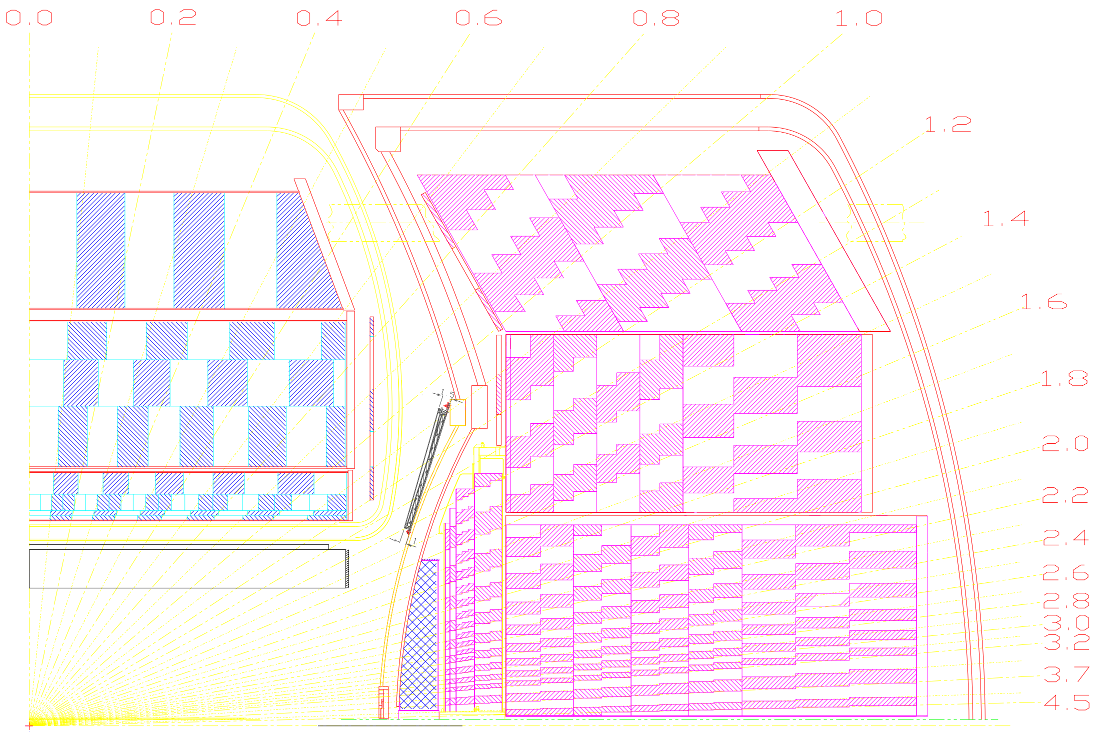

Figure 2.8: Side view of a quarter of the calorimeter, with numbers indicating η values relative to the center of the detector.

electrons and hadrons through their shower profiles.

The DØ calorimeter has a “pseudo-projective” set of readout towers (see Fig. 2.8), with each tower subdivided in depth so that the *centers* of cells of increasing shower depth lie on rays projecting from the center of the interaction region, but the cell boundaries are perpendicular to the beam axis. Figure 2.8 shows the side view of the segmentation of the DØ calorimeter. EM modules have four layers in depth in both the CC and EC. The first two layers reflect the longitudinal shower development near the beginning of the shower, where photons and π^0s differ statistically after ≈ 2 radiation lengths (X_0) of material. The third layers of EM modules usually contain the maximum EM-shower depositions, and have twice the usual segmentation in both η and ϕ, which provides more precise location of EM showers. The fourth layer completes the EM coverage at 20 radiation lengths (X_0). Fine hadronic sections have 3 or 4 layers, and coarse hadronic modules consist of one or three layers. The transverse size of towers in both EM and hadronic modules are $\Delta\eta = 0.1$ and $\Delta\phi = 2\pi/64 \approx 0.1$ (with the third EM layers corresponding to $\Delta\eta \approx \Delta\phi \approx 0.05$).

The new calorimeter electronics were designed to accommodate the Run II bunch spacing (396 ns), but to maintain the Run I noise and pile-up performance. This meant that the analog output signal had to be stored for 4 μs. The Level 1 trigger decision was provided from generation of a separate, fast trigger signal from the calorimeter that was included in the Level 1 trigger level, and required new strategies for baseline subtraction [18].

2.2.4 Muon Detectors

The muon system in Run II was upgraded for the higher expected event rates and backgrounds [16]. The motivation for going to highest luminosities is to study rare processes, such as top quark and W/Z production, and to search for new phenomena. To maximize the acceptance for muons, the detector coverage was extended to $|\eta|$ <2, and made more efficient for unprescaled triggers.

Triggering in the high-rate environment of Run II needed the use of fast trigger elements with good time resolution. In the central $|\eta| < 1$ region, the proportional drift tubes (PDT) used in Run I, with a maximum drift time of 750 ns, were implemented with scintillators that provide the time stamp needed for 396 ns bunch spacings, but the front-end electronics had to be replaced to support deadtimeless operation. Layers of scintillation counters were added just outside of the calorimeter to provide the timing information for matching the muon tracks in the CFT with signals from the PDTs. The scintillator time resolution of 1.6 ns provides good rejection of out-of-time backgrounds.

The forward proportional drift tubes from Run I were replaced with mini drift tubes (MDT) in Run II. The forward muon system consists of three layers of MDTs and three layers of scintillation counters covering $1 < |\eta| < 2$. The MDTs have 1 cm × 1 cm cells, produced in 8-cell extrusions and use a fast gas (90% CF_4 - 10% CH_4) with a drift time of 60 ns [14]. New shielding, consisting of 39 cm of iron hadron and electromagnetic absorber, 15 cm of polyethylene to interact and absorb neutrons, and 15 cm of lead to absorb γ rays, were introduced to reject backgrounds from beam halo, scattered p and $\overline{p}$ fragments interacting in the calorimeter or in the quadrupole magnets at large $|\eta|$.

2.2.5 Luminosity Monitor

The Luminosity monitor (LM) is designed to provide a precise measurement of the rate for non-diffractive inelastic collisions, with high efficiency for making an accurate determination of luminosity at DØ [19]. The secondary purpose of the luminosity monitor is to provide diagnostic information regarding accelerator performance. In addition, the precise ($\approx$ 200 ps) time-of-flight resolution of the LM provides a means for discriminating beam-beam interactions from the principal background from beam-halo interactions, as well as a measure of the position of the primary interaction vertex, and presence of multiple interactions. The luminosity monitor also provides trigger signals to identify beam crossings containing a single $p\overline{p}$ interaction at large $|\eta|$ to determine the presence of hard-diffractive and rapidity-gap triggers [20].

The DØ luminosity monitor for Run II employs plastic scintillators that are read out via photomultipliers. There are 24 wedges around the beam pipe, as shown Fig. 2.9, that are mounted on the inner edge of each EC cryostat at $|z| \approx$ 140 cm. These cover the region $2.7 < |\eta| < 4.4$ [19].

A "luminosity block" is the fundamental unit of time for measuring luminosity, and each block is indexed by a luminosity block number (LBN), which increases monotonically throughout Run II. The LBN is incremented at run or store transitions, or after each 60 seconds of a run, with the chosen time span based on

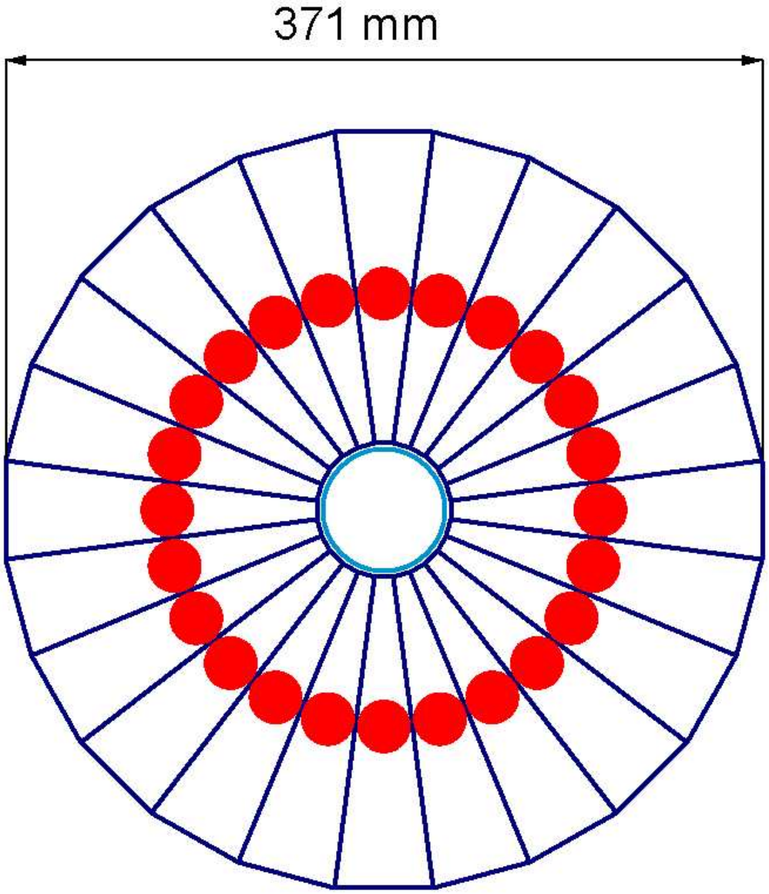

Figure 2.9: The front view of one of the luminosity monitors, with the beam running down the center. The photomultiplier tubes are shown by the filled circles.

constraints in the luminosity, trigger and DAQ systems. This time period is short enough so that the instantaneous luminosity is effectively constant during each LBN. The luminosity is calculated separately for each LBN [19].

2.3 Trigger

The trigger system in DØ detector was upgraded for Run II to enhance data acquisition and triggering to a luminosity of $\mathcal{L} = 2 \times 10^{32}$ cm^{-2}s^{-1}, and 396 ns beam crossings [21].

The Run I DØ trigger system (1992-1996) consisted of two hardware triggers (Level 1 and Level 1.5) and one software trigger (Level 2) [17] to select ≈ 3 Hz of events for further offline processing from ≈ 0.5 MHz collision rate. In Run II, a ten-fold increase of luminosity, and a ten-fold decrease in the time between beam crossings from 3.5 μs to 396 ns required an improved trigger in three basic ways. To increase rejection in L1, the upgraded trigger includes several new tracking detectors: the central fiber tracker (CFT), the central preshower (CPS), the forward preshower (FPS), and the upgraded muon detection system. For L2, which examines all events, several new detector-specific preprocessing engines and a global stage to test for correlations between L1 triggers were implemented [21]. Also, the computational needs of the L3 system were strengthened by improvements in bandwidth and processors. In addition, the L0 system was upgraded, but used primarily as a luminosity monitor.

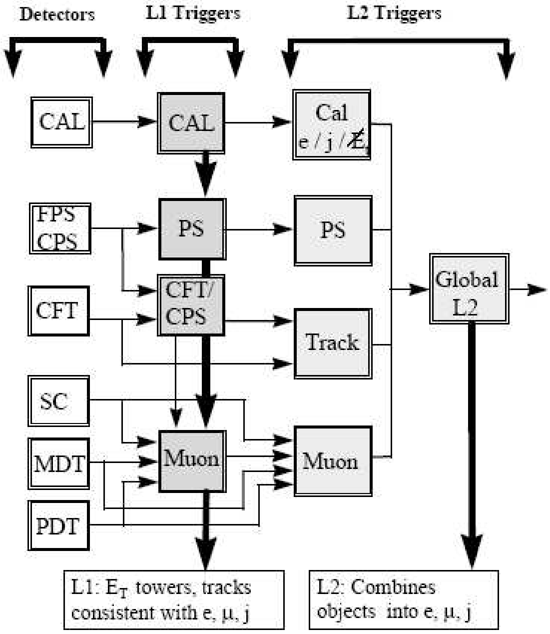

Figure 2.10: L1 and L2 trigger elements, with the horizontal arrows denoting flow of information.

2.3.1 Level 1

The upgraded detectors are shown by the trigger inputs in Fig. 2.10 [21]. The muon system includes a layer of tracking and scintillator planes, a second magnetic spectrometer, and additional layers of tracking at larger radii. The calorimeter, CFT and preshower detectors cover triggering on electrons for $|\eta| < 2.5$, and the CFT and muon systems provide triggering on muons in the region of $|\eta| < 2$.

The L1 triggers associated with each of the trigger detectors examine each event, and pass the information or “trigger terms” to the L1 Framework (L1FW). Each front-end digitizing crate includes sufficient memory to retain data from 36 crossings, which ensures deadtimeless operation. The L1FW examines the list of terms collected from the luminosity monitor, CFT/CPS, FPS, CAL and MUON L1 triggers to determine if a specific L1 bit is satisfied, and then issues an accept for the data to be digitized and moved from the pipeline into a series of 16 event buffers to await the L2 trigger decision. The L1 accept rate is 10 kHz, and the trigger decision is issued 4.2 μs following a beam-beam crossing [21].

2.3.2 Level 2

The accept event rate in Level 2 is reduced to 1 kHz (by roughly a factor of ten) within 100 μs, using multi-detector correlations of signals. There are two distinct L2 stages. The first stage, or preprocessor stage, prepares data from each L1 trigger for use in the second or global processor stage. In the global processor, the combination of L1 trigger objects from different detectors is used as shown in Fig. 2.10. Upon receipt of a L1 accept from the global processor, L2 initializes detector readout, and moves data into eight transfer buffers. There is a one-to-one mapping between the L1 and L2 bits. The global processor receives preprocessor information at 320 Mbytes/s, within a 75 μs trigger decision time, which is based on correlations among multiple detector systems, such as spatial correlations between track segments, preshower depositions, and calorimeter energy depositions for electron candidates [21].

2.3.3 Level 3

The L3 system for Run II has been enhanced to an input rate of 1 kHz and a 50 Hz accept rate, with increases in bandwidth for typical event size of 250 kbytes. The increased rate is achieved with a highly parallelized data pathway and fast processors [21]. Both Run I and Run II systems are characterized by parallel data paths that transfer data from front-end crates to a farm of processors, with each event examined by a processor with a suite of filters. Each front-end crate generates one block of data per event, and these data blocks move independently through the data system and are recombined into single events at their assigned L3 processor nodes. With additional controllers and processors, the system bandwidth can be increased to 10 kHz. Using high-level programming or event filtering, rate rejection is achieved by filtering each event with "physics tools", and these tools access all the data to search for electron, muon, and jet candidates, as well as any interesting event topologies. Finally, any event meeting filter requirements is transferred at about a 50 Hz rate to tape storage for later offline reconstruction.

Chapter 3

Data Reconstruction and Simulation

3.1 Triggers for Event Selection

As described in Section 2.2.2, DØ has a three-tiered trigger system to select potentially interesting events. The information from different subdetector systems is provided at an input rate of 7.5 MHz, and these three trigger systems reduce the event rate to 50 Hz. The Level 1 trigger elements are denoted by CEM(n, x) and CJT(m, y), based on information from the calorimeter. CEM(n, x) and CJT(m, y) reflect the presence (or requirement) of n or m trigger towers with some minimum amount of electromagnetic or total (sum of electromagnetic and hadronic) energy

Trigger Version	v8-11(7/2002-7/2003)	v12(7/2003-7/2004)
Trigger Name	EM15_2JT15	E1_SHT15_2J20
L1	CEM(1,10)CJT(2,5)	CEM(1,11)
L2	EM(.85,10)JET(2,10)	–
L3	ELE_SHT(1,15)JET(2,15)	ELE_SHT(1,15)JET(2,20)

Table 3.1: Summary of triggers for trigger lists v8–12, for the time periods specified in the parentheses on the first line.

specified by x or y in GeV. The notation for Level 2 information corresponds to EM(f, x) and JET(n, y), where f is the fraction of electromagnetic energy relative to total energy in the calorimeter, with a minimum amount of electromagnetic energy specified by x GeV, and n jet candidates with a minimum amount of total (sum of electromagnetic and hadronic) energy y GeV. The L3 condition ELE_SHT(1,15)JET(2,15) indicates a requirement that at least one electron passes a shower-shape comparison, for an energy threshold greater than 15 GeV, and 2 jet candidates have a minimum amount of total (sum of) electromagnetic and hadronic energy of 15 GeV. The data used in this analysis were recorded on the basis of five trigger lists (v8 to v12) to select top-like events. Table 3.1 gives a summary of trigger requirements for this analysis. All these criteria were studied in great detail, and their impact on data can be found in Ref [23].

3.1.1 Single-Object Trigger Efficiency

The trigger efficiencies for selecting single objects (electrons or jets) are parameterized as a function of the kinematic variables transverse momentum (p_T), η and ϕ of the objects reconstructed offline, as based on unbiased samples of data that are required to pass the trigger selections of interest.

Electrons

The efficiency for triggering on an electron is obtained from a sample of $Z \rightarrow e^+e^-$ events selected from 2-electron candidates contained within a small window around the Z mass, as specified by the criteria used by the Top Physics group [22]. The method is the so called "tag-and-probe", which requires one electron chosen randomly ("tag") to satisfy the single electron trigger selection, and uses the other electron to check whether it too satisfies the electron trigger criterion (see Ref. [23] for detail).

Jets

The trigger efficiencies for jets are parameterized as a function of jet p_T in three regions of the calorimeter: CC $|\eta| < 0.8$, ICR $0.8 \leq |\eta| \leq 1.5$, and EC $|\eta| > 1.5$ (ICR corresponds to the region of poor resolution between the CC and EC). The jet trigger efficiency is measured using a sample of events that satisfied any single-electron triggers, but in order to reduce the contamination from true electrons, only events that passed the L1 and L2 electron trigger requirement were considered (see Ref. [23] for detail).

3.1.2 e+jets Triggers

The trigger efficiency for e+jets is measured by combining single-object trigger efficiencies [23]. The total event probability P(L1,L2,L3) is defined as :

$$P(L1, L2, L3) = P(L1) \cdot P(L2|L1) \cdot P(L3|L1, L2) \tag{3.1}$$

where the two probabilities $P(L2|L1)$ and $P(L3|L1, L2)$ on the right are conditional.

The combined probability for different types of objects can be defined as :

$$P(Object_1, Object_2) = P(Object_1) \cdot P(Object_2) \tag{3.2}$$

assuming that the probability for a single object with a specific trigger condition is independent of other objects. This is a good assumption, as shown in Ref [23]. The probability for e+jets triggers can be obtained from the product of the probability of the event to satisfy the conditions at each trigger Level as presented in Table 3.1:

$$P_{e+jets} = P_{L1} \cdot P_{L2} \cdot P_{L3} \tag{3.3}$$

The total trigger efficiency is therefore obtained from individual single-object trigger efficiencies and found to be 93 ± 3%.

3.1.3 Single-Electron Triggers

For special purposes (e.g., Berends Scaling method in Section 5.2.1) we use single-electron triggers to select control samples. Table 3.2 shows the summary of the requirements for these triggers. These requirements are less restrictive than used for the final sample (Table 3.1).

Trigger Version	v8-11(7/2002-7/2003)	v12(7/2003-7/2004)
Trigger Name	EM_HI_SH	E1_SHT20
L1	CEM(1,10)	CEM(1,11)
L2	–	–
L3	ELE_SHT(1,12)	ELE_SHT(1,20)

Table 3.2: Summary of selections for single-electron triggers used for studies of Berends Scaling for trigger lists v8–12.

3.2 Data Processing and Luminosity

3.2.1 Data Processing

The events passed by the L3 trigger are reconstructed to objects used for physics analysis through the DØ offline reconstruction program (RECO) [24]. This CPU-intensive program processes collider events recorded during online data taking and simulates MC events on the offline production farms, and places the output into the central data storage system (SAM) [27] for further analysis. The output from RECO includes many additional "chunks" associated with each type of reconstructed object as two output formats or data tiers. One is the data summary tier (DST), which contains all information necessary to perform any physics analysis, including limited re-reconstruction of high-level physics objects; and the other is the thumbnail (TMB) [26], which provides a highly concentrated format that can be used directly to perform many analyses, and allows the rapid development of event selection criteria.

The basic reconstruction procedure is as follows. First, hit information digitized from sense wires of the tracking detectors is collected and converted to spatial locations in physical coordinates. Tracks are constructed using the hit information from trackers. Information on energy deposition is collected from calorimeter cells. The muon tracks are reconstructed using the information from muon detectors.

Using these charged tracks and calorimeter clusters, the primary and the secondary vertices are constructed. These vertices, tracks and clustering information are used to identify objects such as jets, electrons, photons, and muons. This is called particle identification, and it is based on selection criteria designed for each object.

The reconstructed data is stored in SAM (Sequential data Access via Metadata). SAM is a file-based data management and access layer between the Storage Management System and the data processing layers [27]. The goal of SAM is to optimize data storage and delivery resources, such as tape mounts, drive usage and network bandwidth.

3.2.2 Luminosity

Since we have increased luminosity over Run I, it takes a longer time and requires more disk space to put data into "ntuple" format [28] for analysis. DØ processes all events from SAM into a thumbnail format, with specific requirements for all physics analyses called the skimming process. For our analyses, we used the events that require at least one electron with rather loose selection criteria, and a matched track from information from the tracker (EM1TRK). Although the Top Group has provided ntuples for analysis [22], we made ntuples directly from skimmed events, using a modified version of the standard analysis package ("top_analyze"). These events differ slightly from the ntuples provided by the Top Group, because jets in the Top Group's ntuples are thrown away if one is matched to a "loose" electron. To handle this properly, we corrected the code to include these events because they should be treated as jets, since loose electrons are mostly not true electrons but rather jets. The luminosity was calculated using the top_dq package, which provides a code to generate and use good luminosity block lists matched to triggers as well as the luminosity calculation for the Top Group data samples [30]. The data was taken during the period between June 2002 and September 2003. The total integrated luminosity recorded was approximately 180 pb^{-1}, and after selecting good quality data, we used about 166 pb^{-1} for this analysis. Table 3.3 summarizes the integrated luminosities. The total uncertainty on the integrated luminosity is estimated to be 6.5% [22].

Trigger List	$\int \mathcal{L}$ (pb^{-1})
v8	20.7
v9	31.1
v10	15.9
v11	56.2
v12	41.9
total	165.9

Table 3.3: Integrated luminosities for the trigger list versions of interest.

3.3 Monte Carlo Simulation

3.3.1 Event Generators

$t\bar{t}$ and W+jets events are generated at $\sqrt{s} = 1.96$ TeV using ALPGEN 1.2 [31], and PYTHIA 6.2 [32] for subsequent hadronization of the ALPGEN partons. CTEQ6.1M in ALPGEN and CTEQ5L in PYTHIA are used for modeling the proton and antiproton parton distributions. In the $t\bar{t}$ simulations, the mass of the top quark is set to 175 GeV [22].

The objective is to provide an accurate representation of event properties that can be used to extract information through a comparison with data. The DØ Monte Carlo (MC) simulation system is based on a combination of analytic results and QCD-based ideas, with different subroutines and functions, switches and parameters, that can be used to improve agreement of MC with a variety of data [33].

W+jets events are simulated using the ALPGEN matrix element, which is more precise than from the VECBOS, although still at leading order [22].

For background from multijet events, in which jets mimic electrons, we use a data sample with small $\not{E}_T$, to minimize confusing this background with true sources of electrons, which often have large $\not{E}_T$. This is done because QCD is not reliable at the level needed for simulating multijet background in e+jets events.

3.3.2 Full Detector Simulation

DØGSTAR [34] is a simulation program based on the CERN program GEANT [35]. We use v3.21 to trace particles through the apparatus and to calculate energy deposition in the detectors, and the digitization program DØSIM [36] to convert the output from DØGSTAR to the same format as the electronic output of the detector, while adding the effects of electronic noise and inefficiency and merging of several events to simulate multiple interactions. The Monte Carlo events generated with these programs can then be processed through the DØRECO program, which reconstructs each object from simulated electronic output of the detector, just as is done with the data.

Chapter 4

Particle Identification

4.1 Electron Selection

For the analysis presented in this thesis, we used only the electrons found in the central calorimeter (CC). This is because $t\bar{t}$ production is mainly central, and most of the objects are emitted at small $|\eta|$.

4.1.1 Reconstruction and Identification of Electromagnetic Clusters

During data reconstruction, electromagnetic (EM) clusters are defined as a set of towers in a cone of radius $R = \sqrt{(\Delta\eta)^2 + (\Delta\phi)^2} = 0.4$ around an initial tower selected on the basis of its energy content in the central calorimeter.

The reconstruction efficiency of EM clusters for data and Monte Carlo is determined from Z→ e^+e^- events, and is found to be 96.0± 0.4 % for CC data, for events in a narrow mass window around the Z peak (80-100 GeV) [22]. The reconstruction efficiency obtained for CC for the Monte Carlo event sample is 97.6 ± 0.1 %. A correction factor is applied to account for this difference [22].

For EM objects, we applied these selection criteria.

- $f_{EM} \equiv E_{EM}/E_{Tot} > 0.9$
- $f_{iso} = \frac{E_{Tot}(R<0.4)-E_{EM}(R<0.2)}{E_{EM}(R<0.2)} < 0.15$
- $\chi^2_{H-Matrix} < 12$

Typical EM showers have a large EM fraction. Thus, we define f_{EM}, where E_{EM} is the cluster energy in the EM section of the calorimeter and E_{Tot} is the total energy in the same cone of $R = 0.4$. Also, the cluster must be isolated, which is reflected in f_{iso}, where $E_{Tot}(R < 0.4)$ is the total energy in the cone of $R = 0.4$ and $E_{EM}(R < 0.2)$ is the cluster energy in the EM section of the calorimeter in the cone of $R = 0.2$. Furthermore, we require $\chi^2 < 12$ (so called "H-Matrix", based on 7 variables that compare the values of the energy deposited in each EM layer and the total energy of the shower in the calorimeter to average distributions obtained from Monte Carlo) for accepted EM showers [40].

The electron identification efficiency for the above criteria, just as the triggering efficiency, is estimated using an unbiased sample of electrons from $Z \to e^+e^-$ events in data. This is done by requiring one well-identified electron (passing the criteria described here and in the next section) on the "tag" side and one EM cluster on the "probe" side. The efficiency is found to be 91.7 ±0.7 % in $Z \to e^+e^-$ data and 96.6 ±0.03 % in $Z \to e^+e^-$ MC events.

To select a cleaner sample of electrons, we require a track associated with the cluster that satisfies $|\Delta\phi_{EM,trk}| < 0.05$ and $|\Delta\eta_{EM,trk}| < 0.05$, where the differences in ϕ and η correspond to those between the track and the EM cluster as measured relative to the center of the detector. We estimate that 90.3±0.6% of the electrons have an associated track in $Z \to e^+e^-$ data and 95.2±0.05% in $Z \to e^+e^-$ MC events.

4.1.2 Electron Confirmation using a Neural Network

Although the EM cluster and the associated track requirements discriminate true electrons from background, nevertheless, the huge multijet background still contaminates the electron sample, and more efficient methods are needed to discriminate against this background. The Top Group at DØ uses a likelihood method for this purpose [37], but we found that the likelihood was not trained for the v12 trigger data, and we therefore made a more restrictive χ^2 selection than used in the likelihood selection. We also used a Neural Network (NN) method to discriminate between multijet background and $t\bar{t}$ signal [38, 39].

The Neural Network is trained using six variables:

- Reconstructed position of the vertex point of the electron in z, referred to as z_e
- η of the electron relative to the center of the detector, η_e
- Distance in R to second closest track to the EM cluster (ΔR_2)
- The shape of E_T/p_T for electron
- Distance of closest approach (DCA) of electron track to vertex (Δz_{DCA})
- The χ^2 probability for a track to overlap with the EM cluster

To discriminate between electrons and jets, we train the NN using multijet background (B) and $Z \rightarrow e^+e^-$ signal (S). Figure 4.1 shows the structure of the Neural Network for these events, and Fig. 4.2 shows the output response of the Neural Network for different similar samples of signal and background events. Optimal selection of electrons is defined by minimizing $\sqrt{N_S + N_B}/N_S$, where N_S and N_B corresponds to the number of signal and background events for any given NN cutoff.

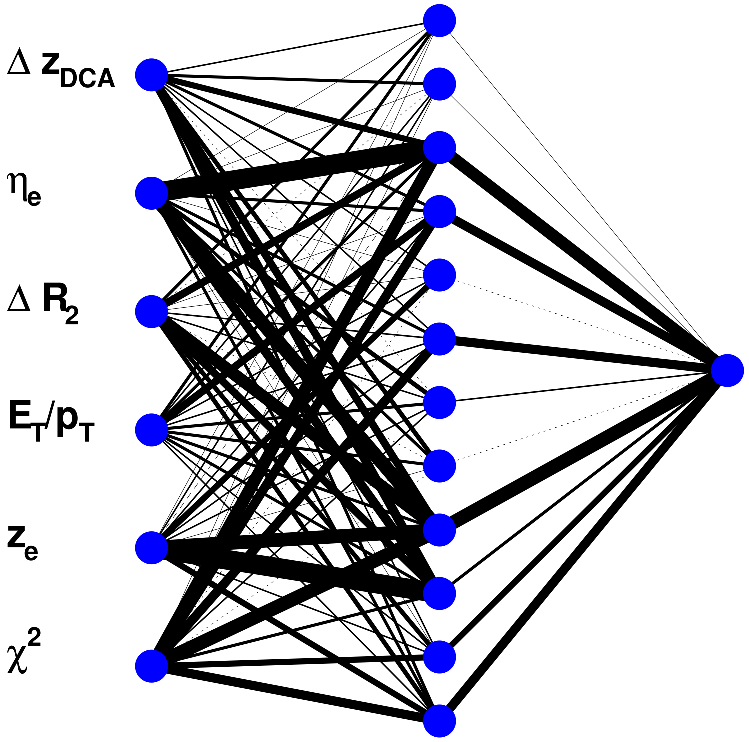

Figure 4.1: The structure of the NN used to select electrons, shown for six input nodes, twelve hidden nodes and one output node. Neurons are depicted by disks, and synapses by lines connecting neurons. The line width is proportional to the weight of the contribution to the decision. The training is for $Z \to e^+e^-$ (MC) and multijet events (data).

Figure 4.3 shows the signal efficiency vs background survival probability as a function of NN cutoff value, where NN = 0.47 corresponds to the minimum in $\sqrt{N_S + N_B}/N_S$, and a signal efficiency of 93.7±0.05% for this minimization for $Z \to e^+e^-$ MC events and 81.5±0.9% for $Z \to e^+e^-$ data.

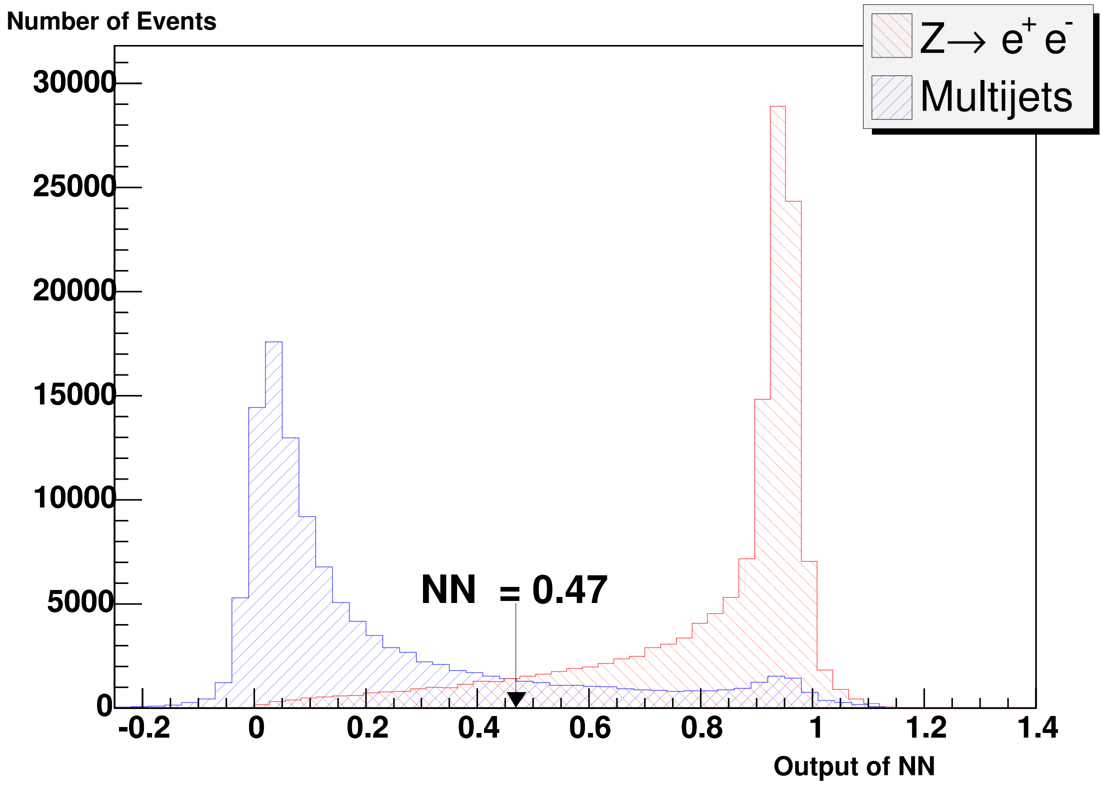

Figure 4.2: The output of the trained Neural Network on two other test samples. Signal corresponds to $Z \rightarrow e^+e^-$ data, and background to multijets. The arrow indicates the optimal NN value (see Fig. 4.3).

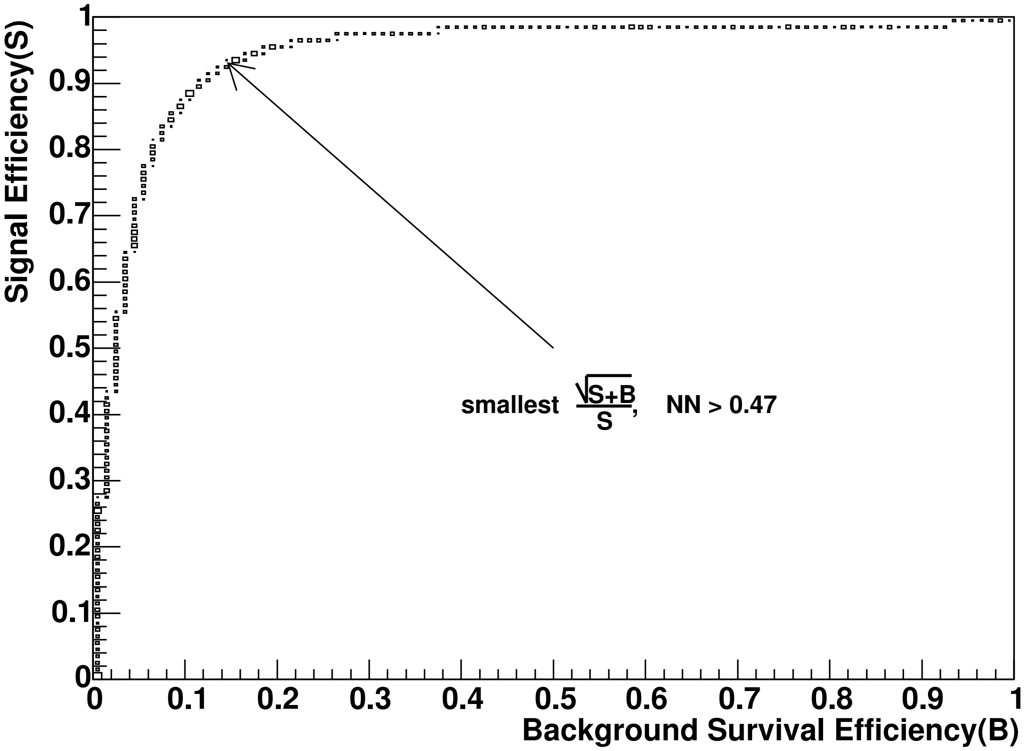

Figure 4.3: Signal vs Background efficiency, and the optimal NN = 0.47 value obtained by minimizing $\sqrt{N_S + N_B}/N_S$.

4.1.3 Electron Energy Resolution

The energy loss in material in front of the calorimeter (solenoid and preshower detectors) was corrected for data using a parameterized dependence as a function of electron η and energy [41].

4.2 Jet Selection

4.2.1 Jet Reconstruction and Identification

A jet cluster in the calorimeter is defined in the "improved legacy cone" algorithm [42] by a cone of R = 0.5. The sum of all cells sharing the same pseudorapidity and azimuthal angle provides seed towers where a tower is the set of cells which together make up a pseudo projective tower. When the total energy of the cluster within 0.5 cone is ≥ 8 GeV, a jet is reconstructed.

For Jet objects, we require these criteria to minimize the contribution from noise and hot cells or fake jets:

- The fraction of energy deposited in the electromagnetic part of the calorimeter (EMF) has to be $0.05 < EMF < 0.95$, to remove isolated electromagnetic particles.
- The fraction of jet energy deposited in any coarse hadronic section of the

calorimeter (CHF) must be CHF < 0.4, to remove jets that are caused by noise in the coarse hadronic sections.

- The ratio of transverse energies in the highest to the next-highest cell in the calorimeter (HotF) must be HotF < 10, to remove jets formed from hot cells.
- To remove jets formed from a single hot tower, 90 % of the jet energy (n90) must be deposited in at least two towers.
- After the coverage and calibration of the L1 calorimeter system was improved following the implementation of trigger version v8 (after Run 172,359) [43], jet confirmation at Level 1 was found to be the most powerful discriminant against noise.

4.2.2 Jet Energy Scale (JES) and Jet Energy Resolution (JER)

Because of nonlinearities, dead material, noise and showering effects, the measured energy in a jet cone is not equal to the original energy of the particles in the calorimetric shower. The measured jet energy (E_{meas}) must therefore be corrected to the energy of the emitted particles (E_{corr}) before they interact in the calorimeter. This correction factor is often referred to as the jet energy scale (JES) correction, which can be written as [22]:

$$E_{corr} = \frac{E_{meas} - O}{R \times S} \tag{4.1}$$

where R is the calorimeter response to a jet, determined by balancing E_T using the observed $\not\!\!E_T$ in γ+jets events, and O is the energy offset due to the underlying event, energy pile-up, multiple interactions, electronic noise and uranium noise caused by radioactivity from the uranium absorber. O is determined from energy densities found in minimum-bias events, and S is the fraction of the shower that leaks outside the jet cone in the calorimeter. (It should be recognized that the JES correction has nothing to do with any possible correction of jets to their parton progenitors.)

Dijet event samples are used for the measurement of jet energy resolution (JER) for high energy jets ($E_T \gtrsim 50$ GeV). By measuring the asymmetry variable $\mathcal{A}$ in the sample, defined as :

$$\mathcal{A} = \frac{|p_{T1}| - |p_{T2}|}{|p_{T1}| + |p_{T2}|} \tag{4.2}$$

the jet transverse energy resolution can be determined from the width of the distribution in $\mathcal{A}$ (δ_A). Assuming a Gaussian form [22], it follows that :

$$\frac{\delta_{p_T}}{p_T} = \sqrt{2}\delta_{\mathcal{A}} \tag{4.3}$$

4.3 Missing Transverse Energy $\not\!\!E_T$

The missing transverse energy $\not\!\!E_T$ is the imbalance in transverse momentum in the event. Since the response of electromagnetic particles such as photons, electrons or π^0 mesons is different from that of jets [44], which largely contain hadrons, the imbalance from electromagnetic objects and jets results in a finite missing transverse energy ($\not\!\!E_T$). This is very important for determining the possible presence of a neutrino in an event, as expected from top decays. $\not\!\!E_T$ is reconstructed from the vector sum of the transverse energies of all cells, except those in the coarse hadronic layer due to their high level of noise. To calculate the summed $\not\!\!E_T$, for the coarse hadronic calorimeter we use only cells clustered within good jets.

4.4 Vertex Selection

The primary vertex (PV) is reconstructed in DØRECO using all tracks in the SMT and CFT [45]. Additionally, for a high-quality reconstructed vertex [47], we require that the PV in z (PV_z) is within the fiducial region of the SMT ($|PV_z| \leq$

60 cm), and have at least three tracks ($N_{tr} \geq 3$) associated with it. The efficiency for these selections can be obtained from $Z \rightarrow e^+e^-$ data and the $t\bar{t}$ MC sample, corrected for topological differences between Z data and $t\bar{t}$ events, using the ratio of efficiencies measured in the corresponding Monte Carlo samples. For $Z \rightarrow e^+e^-$ events, this is found to be 98.9±0.8% [47]. We assume the same efficiency for the e+jets channel from $t\bar{t}$ events, where we also require the distance between the PV and the vertex of the electron to be $\Delta z(e, PV) < 1$ cm, to ensure that the electron comes from the decay of a W (which is the decay product of $t\bar{t}$). This efficiency is found to be 96.4±0.1% from the $t\bar{t}$ MC sample.

Chapter 5

Event Selection and Analysis

The signature for $t\bar{t}$ events with e+jets in the final state corresponds to one isolated electron with high transverse momentum, a large $\not\!\!E_T$, and four or more jets. Since the signature is similar to that for W+jets production, the primary physics backgrounds are W+jets production. The signature for signal relative to background is improved by requiring 4 or more jets with a good high-p_T electron. The greatest differences between signal and background is in the event topology and the presence of b quarks in $t\bar{t}$ events. DØ has developed several methods to detect b quarks, such as soft-muon tagging or secondary-vertex tagging, but in this analysis we measure the $t\bar{t}$ cross section using just the character of the event topologies, employing either a Random Grid Search [46] or Neural Network (NN) [39] discrimination. This provides more events, but contains higher background contamination than methods based on b tagging.

Also we have to consider multijet ("QCD") events with one jet misidentified as an electron and mismeasured to produce an effective $\not\!\!E_T$ as instrumental backgrounds [4].

Using the basic particle identification described in Chapter 4, therefore, we perform a preselection designed to enrich $t\bar{t}$ and W+jet events and to suppress multijet events in the data. A summary of the preselections is given in Table 5.1. The less restrictive electron selection ("loose") is used to evaluate multijet backgrounds in preselected events, and is discussed in the following section. The tighter electron selection requires the EM candidate to pass certain additional Neural-Network selections appropriate for true electrons, and was described in Chapter 4. The requirement that the azimuth angle between the direction of the electron and $\not\!\!E_T$ be large ($\Delta\phi(e,\not\!\!E_T) > 0.5$) is used to suppress events in which $\not\!\!E_T$ arises from downward energy fluctuations in jets mimicking electrons [47].

Loose selection criteria
$E_T^e > 20$ GeV & $\lvert\eta^e\rvert < 1.1$ (CC)
$E_T^{jet} > 15$ GeV (20 GeV for leading Jet) & $\lvert\eta^{jet}\rvert < 2.5$
$\not\!\!E_T > 20$ GeV & $\Delta\phi(e,\not\!\!E_T) > 0.5$
$N_{trk}(PV) \geq 3$ & $\Delta z(e, PV) < 1$ cm & $\Delta z(PV) < 60$ cm
Tight selection criteria
Loose selection & Neural-Network confirmation for electron

Table 5.1: Loose and tight selection criteria in e+jets channel.

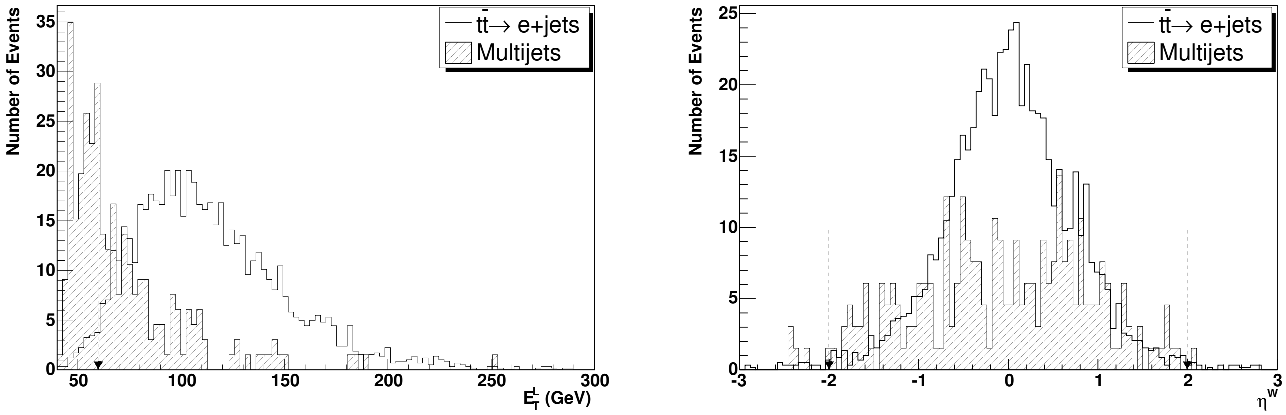

Figure 5.1: Distributions in E_T^L and η^W, based on simulations of $t\bar{t}$ production and multijet data. Dashed arrows indicated the additional selections made to reduce multijet background.

To reduce background from multijet events, in addition to the above preselection criteria, we further require $E_T^L > 60$ GeV and $|\eta^W| < 2.0$, before proceeding with the Random Grid Search or Neural Network. The criteria are justified in the distributions shown in Fig. 5.1. (E_T^L is defined as the sum of E_T of the electron and of $\not\!\!E_T$, and η^W as η of the W boson, assuming the momentum of the electron and $\not\!\!E_T$ for the neutrino.) The criterion on η^W is not very important, and has primarily historic origin [49].

With preselected events, in the RGS analysis, we estimate W+jet production backgrounds assuming "Berends Scaling" [48], and define $t\bar{t}$ events based on a Random Grid Search (RGS) of cutoffs on variables that minimize the uncertainty on the $t\bar{t}$ cross section. In the NN analysis, we determine the number of $t\bar{t}$ and background events directly from a fit to the output of a Neural Network.

5.1 Instrumental Background : Multijet Events

The preselected sample includes W+jets and $t\bar{t}$ as well as multijet events. The multijet portion in the sample can be estimated by using two event samples: (i) a loose electron sample (N_ℓ), and (ii) a tight electron sample (N_t), which is a subset of the loose sample. A procedure called "Matrix Method" was developed in Run I (but not used for top analysis), but has been applied in top analyses in Run II [49] to extract the multijet background in lepton+jets events.

We can define ε_{sig} as the rate for W+jets and $t\bar{t}$ events to pass some specified selections, and ε_{QCD} as the rate for multijet events to pass the same selection, e.g. from the loose set to the tight set. The total number of signal and background events are denoted $N^{W+t\bar{t}}$ and N^{QCD}, respectively. N_ℓ and N_t, corresponding to the number of events in the loose and tight samples after preselection, can be written as :

$$N_\ell = N^{W+t\bar{t}} + N^{QCD} \tag{5.1}$$

$$N_t = \varepsilon_{sig} N^{W+t\bar{t}} + \varepsilon_{QCD} N^{QCD} \tag{5.2}$$

where ε_{sig} and ε_{QCD} are the efficiencies for W+jets and $t\bar{t}$ events and the efficiencies for multijet events to pass the tight electron requirements, respectively.

These two linear equation can be solved to yield :

$$N^{W+t\bar{t}} = \frac{N_t - \varepsilon_{QCD} N_\ell}{\varepsilon_{sig} - \varepsilon_{QCD}} \tag{5.3}$$

$$N^{QCD} = \frac{\varepsilon_{sig} N_\ell - N_t}{\varepsilon_{sig} - \varepsilon_{QCD}} \tag{5.4}$$

and we can therefore estimate $N^{W+t\bar{t}}$ and N^{QCD} in the preselected sample.

The precise values of ε_{sig} and ε_{QCD} are crucial for the success of this method. We estimated ε_{sig} using $Z \to e^+e^-$ events, as shown in Table 5.2. Since $Z \to e^+e^-$ production has very few events with high jet multiplicities ($N_{jets} \geq 3$), we have to rely on events with $N < 3$ multiplicities. For the matrix method, we use ε_{sig} obtained for the Z+1 jet multiplicity, but ε_{sig} for different jet multiplicities is consistent with this within error. ε_{QCD} can be obtained from higher jet multiplicities, where the appropriate event sample corresponds to our loose sample, except that we require $\not{E}_T < 10$ GeV, because in this region we do not expect true electrons from $t\bar{t}$ or W+jets production but mainly jets misidentified as electrons. ε_{QCD} is shown for each jet multiplicity and different trigger versions in the last column of Table 5.3. ε_{sig} is not sensitive to different trigger versions [47], and we therefore estimate its value independent of trigger version.

For the matrix method, we use the ε_{QCD} appropriate for each jet multiplicity. The extracted ε_{QCD} values are shown by the constant values at $\not{E}_T < 10$ GeV in Figs. 5.2 and 5.3. That is, since we require $\not{E}_T < 10$ GeV for each jet multiplicity, a fit to a constant at small $\not{E}_T$ for each jet multiplicity provides ε_{QCD}. Although there appears to be some possible disagreement for a constant ε_{QCD} at $\not{E}_T < 10$ GeV for $N_{jets} \geq 4$, the statistics are too poor to come to a definite conclusion. Figures 5.4 and 5.5 show ε_{QCD} as a function of jet multiplicity and trigger.

N_{jets}	N_ℓ	N_t	ε_{sig}
$\geq$0	11222	9315	0.830±0.004
$\geq$1	1980	1613	0.815±0.009
$\geq$2	363	287	0.791±0.021

Table 5.2: ε_{sig} extracted from $Z \rightarrow e^+e^-$ events.

A summary of the results from the Matrix Method is shown in Table 5.3, where jet multiplicity N_{jets} refers to an inclusive jet multiplicity ($\geq N_{jets}$).

Triggers	N_{jets}	N_ℓ	N_t	$\varepsilon_{sig}N^{W+t\bar{t}}$	$\varepsilon_{QCD}N^{QCD}$	ε_{QCD}
v8-11	$\geq$1	11862	6684	5981$\pm$105	703$\pm$34	0.156$\pm$0.002
	$\geq$2	4777	2186	1789$\pm$60	397$\pm$21	0.154$\pm$0.004
	$\geq$3	1304	506	394 $\pm$29	112$\pm$11	0.136$\pm$0.008
	$\geq$4	293	112	99 $\pm$12	13 $\pm$3	0.075$\pm$0.015
v12	$\geq$1	3093	1184	1711$\pm$57	173$\pm$19	0.174$\pm$0.004
	$\geq$2	1214	655	571$\pm$33	84$\pm$11	0.163$\pm$0.008
	$\geq$3	355	173	153$\pm$16	20$\pm$5	0.121$\pm$0.017
	$\geq$4	77	41	37$\pm$8	4$\pm$2	0.116$\pm$0.041

Table 5.3: Summary of results from preselection and the Matrix Method. ε_{QCD} is estimated using multijet events for different trigger versions.

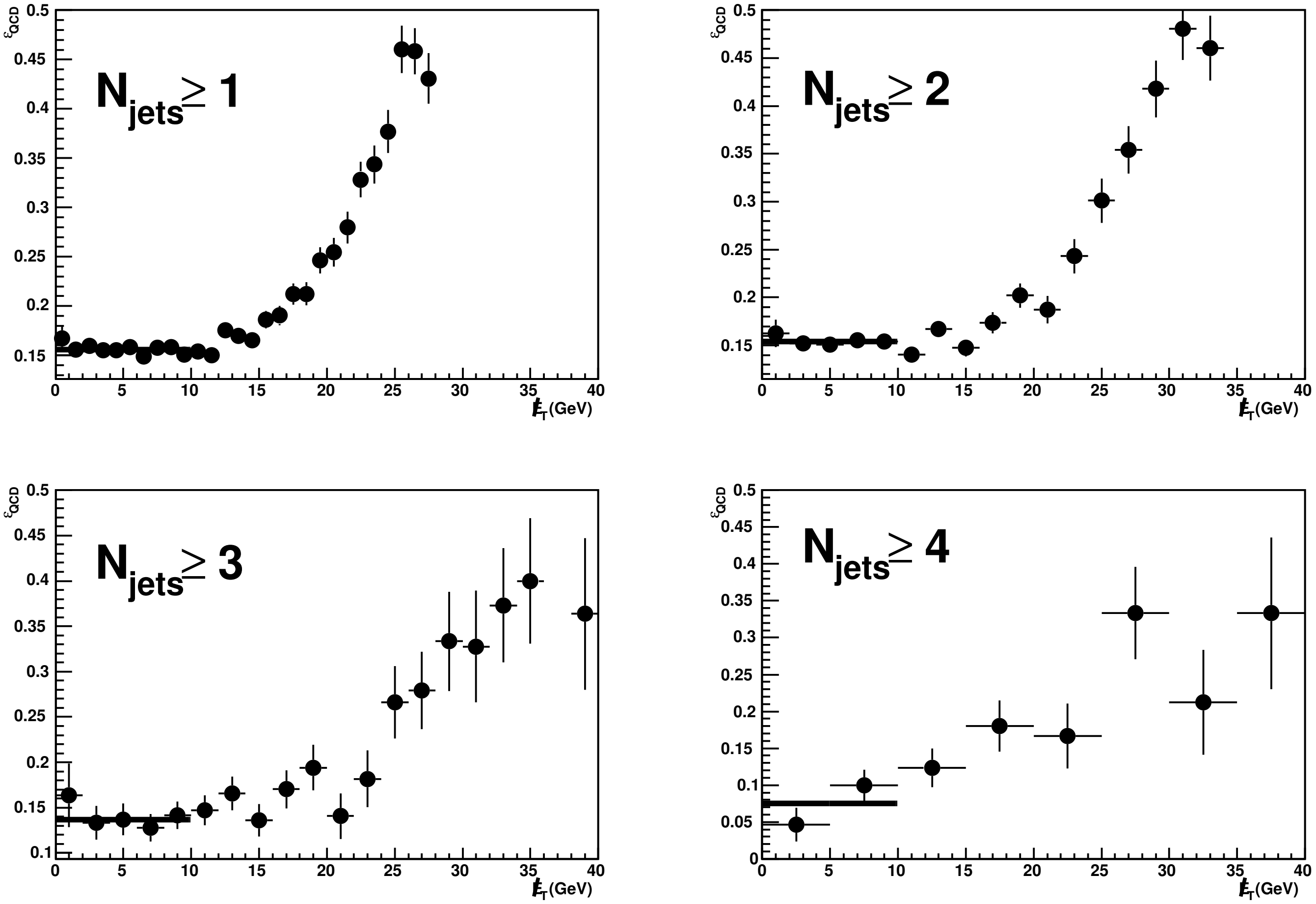

Figure 5.2: ε_{QCD} as a function of $\not\!\!E_T$ and inclusive N_{jets} for v8-11 versions of the trigger. Data for $\not\!\!E_T < 10$ GeV is used to estimate ε_{QCD}.

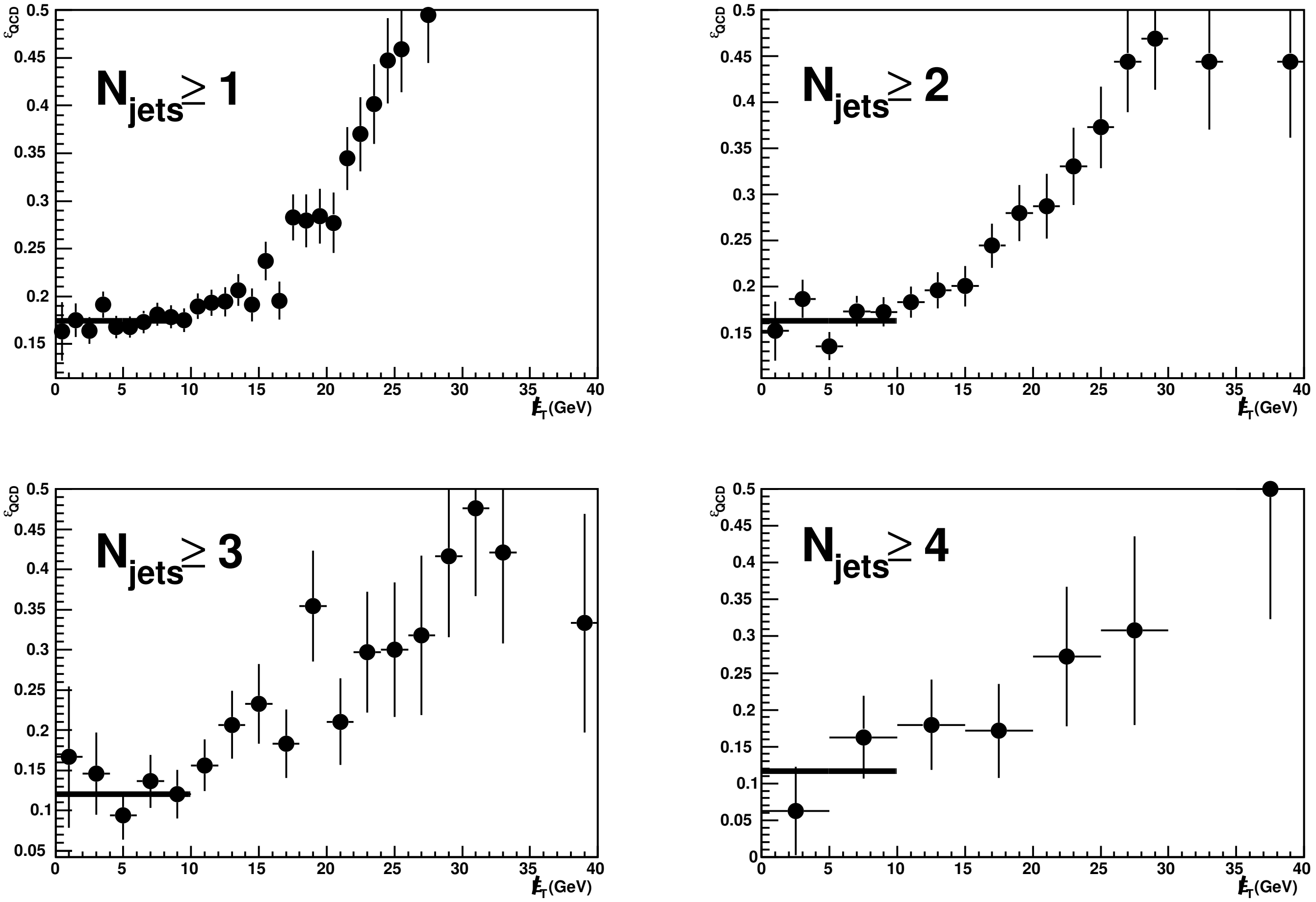

Figure 5.3: ε_{QCD} as a function of $\not\!\!E_T$ for the v12 trigger version (events with $\not\!\!E_T <$ 10 GeV are used to estimate ε_{QCD}).

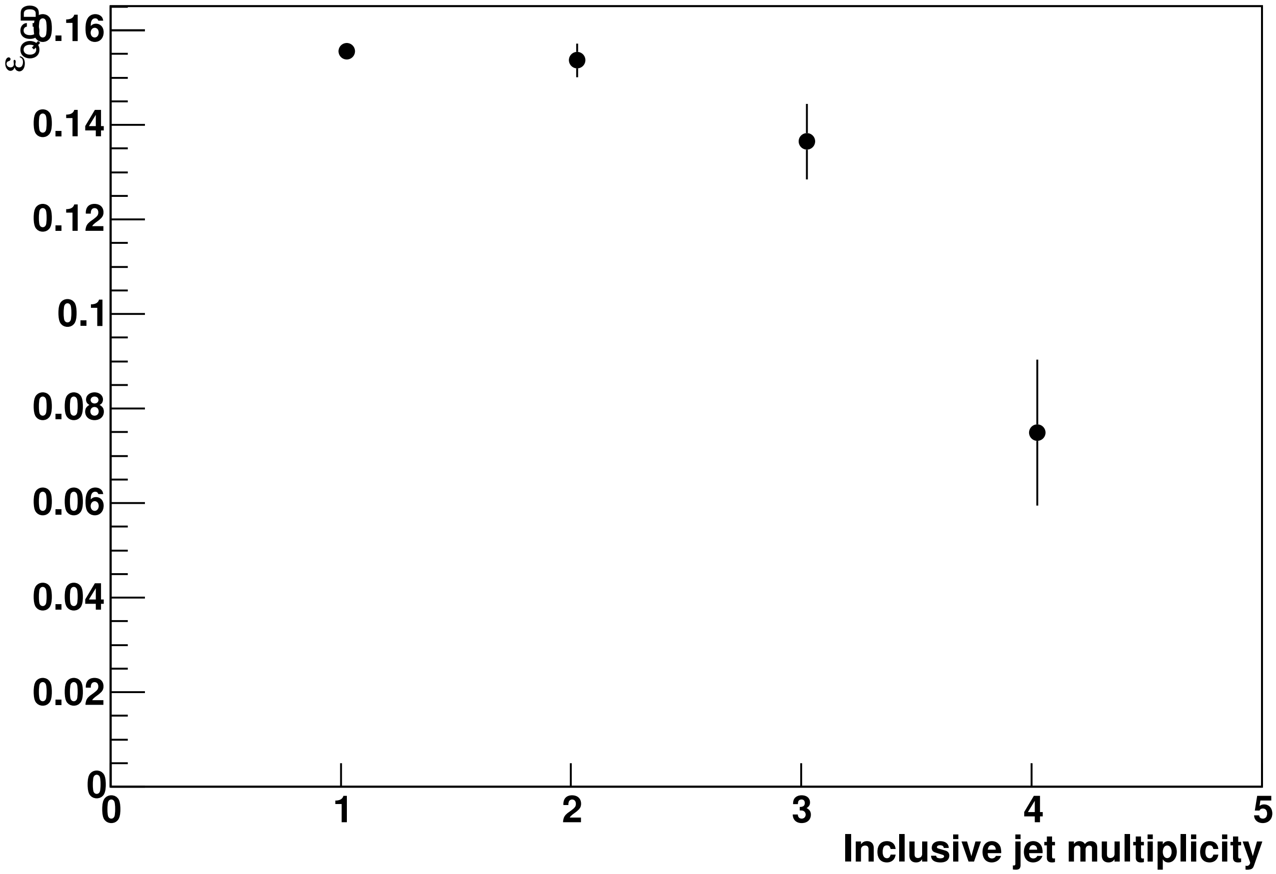

Figure 5.4: ε_{QCD} as a function of N_{jets} for v8-11 trigger versions.

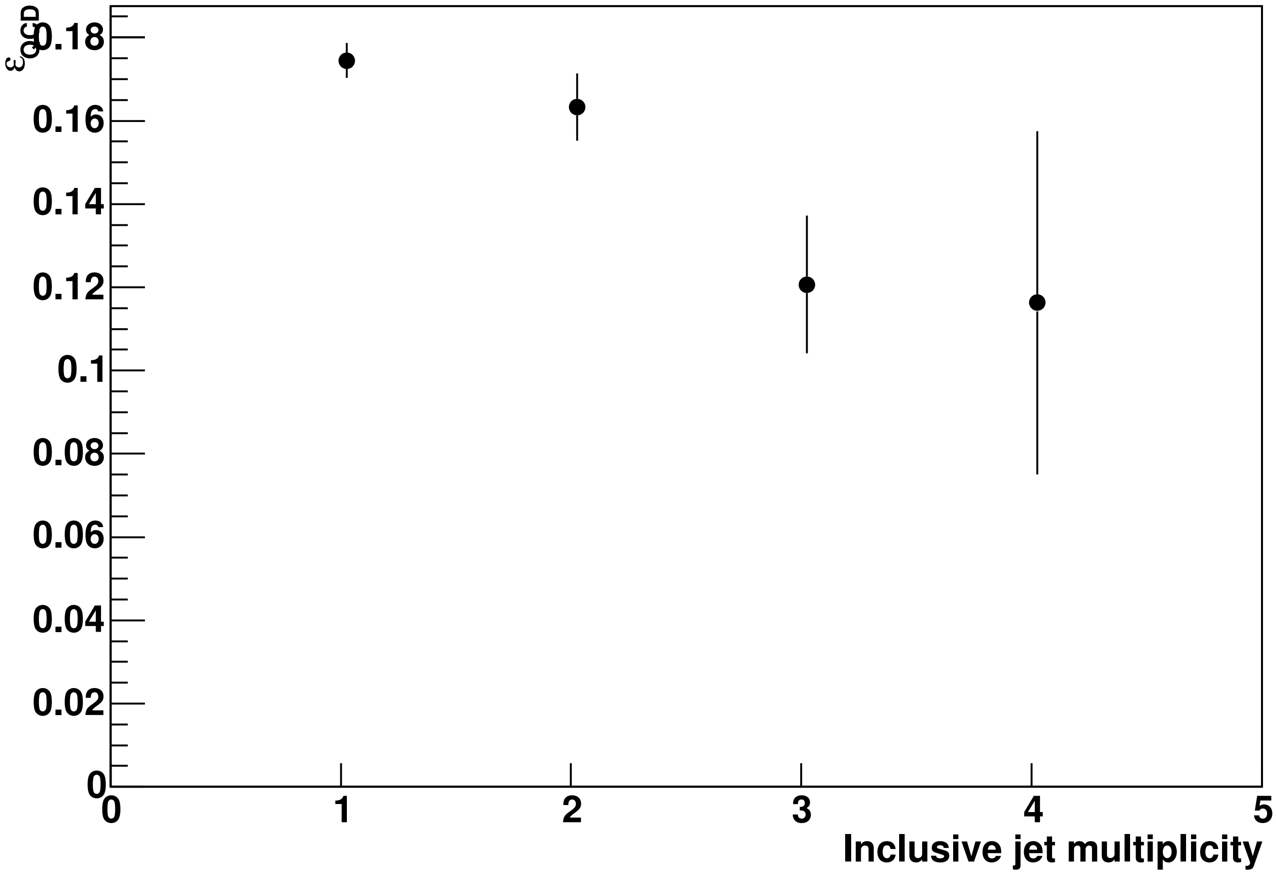

Figure 5.5: ε_{QCD} as a function of N_{jets} for the v12 trigger version.

5.2 Physics Background : W+Jets Events

5.2.1 Random Grid Search

Berends Scaling

After subtraction of the multijet background via the Matrix Method, the background from W+jets production is estimated by performing a fit to the jet multiplicity spectrum of the preselected tight electron sample. This fit is based on the assumption of Berends (N_{jets}) Scaling [4], which assumes an exponential dependence of the cross section (or the number of events) for W+jets on the inclusive jet multiplicity N_{jets} :

$$\frac{\sigma(W + (N+1)_{jets})}{\sigma(W + N_{jets})} = \alpha \tag{5.5}$$

where α is a constant (for any given set of jet E_T and η requirements). The number of W+jets events observed for the *ith* inclusive jet multiplicity (after multijet subtraction) is given by

$$N_i^{obs} = N_1^W \cdot \alpha^{i-1} + a_i^{t\bar{t}} \cdot \sigma_{t\bar{t}} \cdot \mathcal{L} \tag{5.6}$$

where N_1^W is the number of W+1 jet events, $\sigma_{t\bar{t}}$ is the unknown cross section for $t\bar{t}$ production, $\mathcal{L}$ is the total luminosity, and $a_i^{t\bar{t}}$ is the acceptance for $t\bar{t}$ events with an inclusive jet multiplicity i, as obtained from Monte Carlo (See Table 5.4). The values of the fit parameters α and $\sigma_{t\bar{t}}$ are extracted from the fit to the data.

Although to enhance the signal and reduce the background we require both electrons and jets in the triggers (see Section 3.1), for applying Berends scaling we require just the electron in the trigger, which minimizes bias from the accompanying jets in the W+jets events. We therefore select separately for this purpose a control sample requiring only electrons in the trigger (all other requirements being the same). The result for N_i^{obs} are given in Figs. 5.6 and 5.7, and these fits to Eq. 5.6 provide the extracted value of α (and a poor measure of $\sigma_{t\bar{t}}$).

The number of W+4 jet events can be estimated from N_4^W as follows :

$$N_4'^W = N_1'^W \cdot \alpha'^3 \tag{5.7}$$

where $N_4'^W$ is the number of W+jets events with 4 or more jets that pass just the electron trigger requirements, where the prime indicates the control sample (only electron trigger).

If we define ε_i^T as the trigger efficiency (bias) of the electron+jet triggers relative to the electron triggers in inclusive jet multiplicities $N_{jets} \geq i$, from the definition

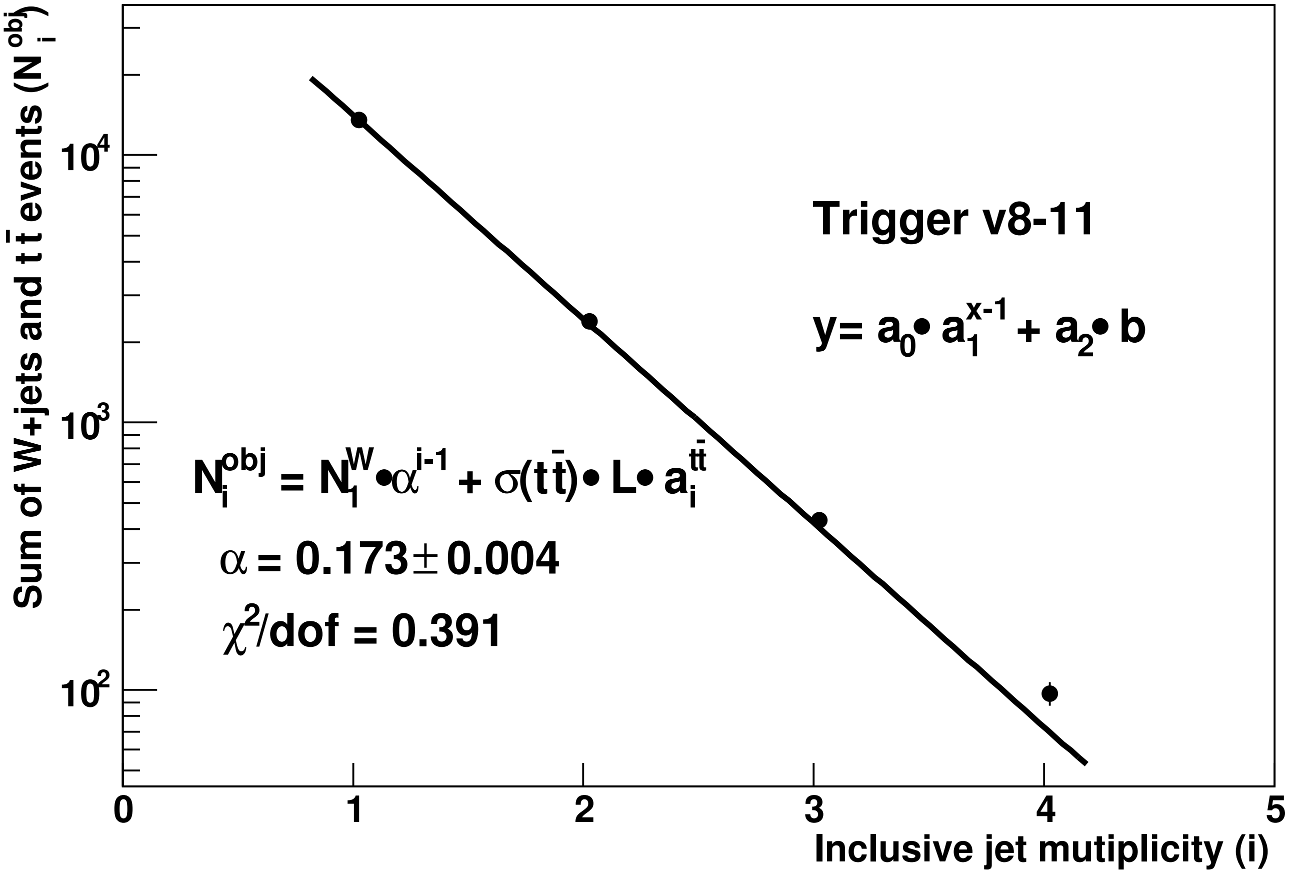

Figure 5.6: A fit assuming Berends Scaling for W+jets , for v8-11 trigger versions for only electron triggers.

of ε_i^T, we can write

$$N_i^W = N_i'^W \varepsilon_i^T \tag{5.8}$$

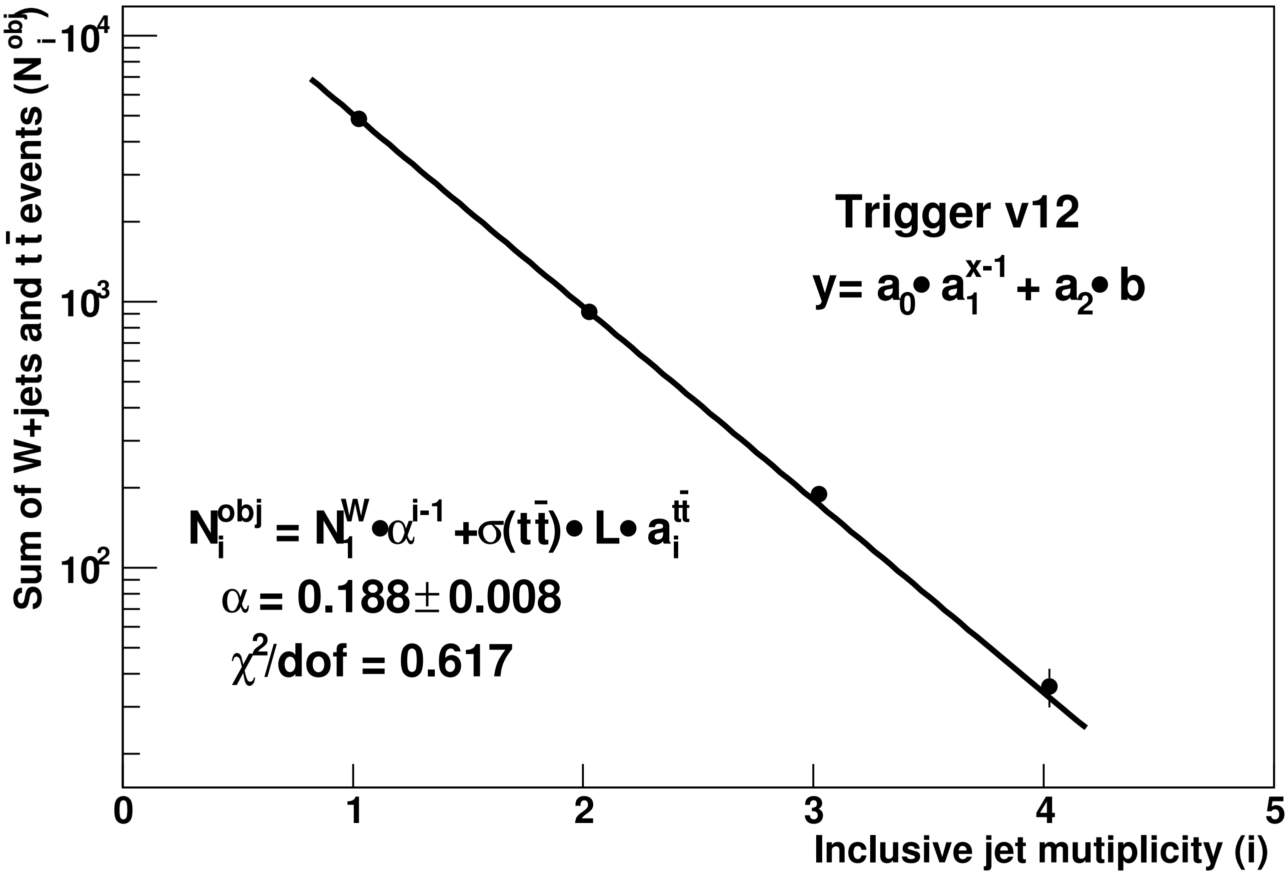

Figure 5.7: A fit to Berends Scaling for W+jets , for v12 trigger version for only electron triggers.

In the Berends Scaling, $N_4'^W$ can be written as :

$$N_4'^W = N_3'^W \cdot \alpha' \tag{5.9}$$

Using Eq. 5.8, we can express

$$\frac{N_4^W}{\varepsilon_4^T} = \frac{N_3^W}{\varepsilon_3^T} \cdot \alpha'. \tag{5.10}$$

Therefore N_3^W can be expressed as

$$N_3^W = N_4^W \cdot \frac{\varepsilon_3^T}{\varepsilon_4^T} \cdot \frac{1}{\alpha'} \tag{5.11}$$

From Eq. 5.6, we can write

$$N_3^{obj} = N_3^W + \sigma_{t\bar{t}} \cdot \mathcal{L} \cdot a_3^{t\bar{t}} \tag{5.12}$$

and

$$N_3^{obj} = N_4^W \cdot \frac{\varepsilon_3^T}{\varepsilon_4^T} \cdot \frac{1}{\alpha'} + \sigma_{t\bar{t}} \cdot \mathcal{L} \cdot a_3^{t\bar{t}} \tag{5.13}$$

by multiplying both sides by α', we obtain :

$$\alpha' \cdot N_3^{obj} = N_4^W \cdot \frac{\varepsilon_3^T}{\varepsilon_4^T} + \alpha' \cdot \sigma_{t\bar{t}} \cdot \mathcal{L} \cdot a_3^{t\bar{t}} \tag{5.14}$$

From Eq. 5.6, we can now write

$$N_4^{obj} = N_4^W + \sigma_{t\bar{t}} \cdot \mathcal{L} \cdot a_4^{t\bar{t}} \tag{5.15}$$

From Eqs. 5.14 and 5.15, for the electron and jets trigger sample, it follows that the relation between the two trigger samples is [50]:

$$N_4^W = \frac{\alpha' \cdot (N_3^{obj} \cdot a_4^{t\bar{t}} - N_4^{obj} \cdot a_3^{t\bar{t}})}{\frac{\varepsilon_3^T}{\varepsilon_4^T} \cdot a_4^{t\bar{t}} - \alpha' \cdot a_3^{t\bar{t}}} \tag{5.16}$$

where N_4^W is the number of W+4 jets events that pass the requirement of having electrons and jets in the trigger, N_3^{obj} and N_4^{obj} is the number of events with inclusive jet multiplicities of 3 and 4, after subtracting multijet events, and ε_3^T and ε_4^T is trigger efficiency (bias) of the electron+jet triggers relative to the electron triggers in $N_{jets} = 3$ and $N_{jets} = 4$ inclusive jet multiplicities, and $a_3^{t\bar{t}}$ and $a_4^{t\bar{t}}$ are the acceptances for $N_{jets} = 3$ and $N_{jets} = 4$ inclusive jet multiplicities. Figures 5.8 and 5.9 show the relative trigger bias by asking that electron triggers pass just the electron+jets trigger requirement. Table 5.4 summarizes the observed values for Eq. 5.16. Table 5.5 summarizes the estimated background.

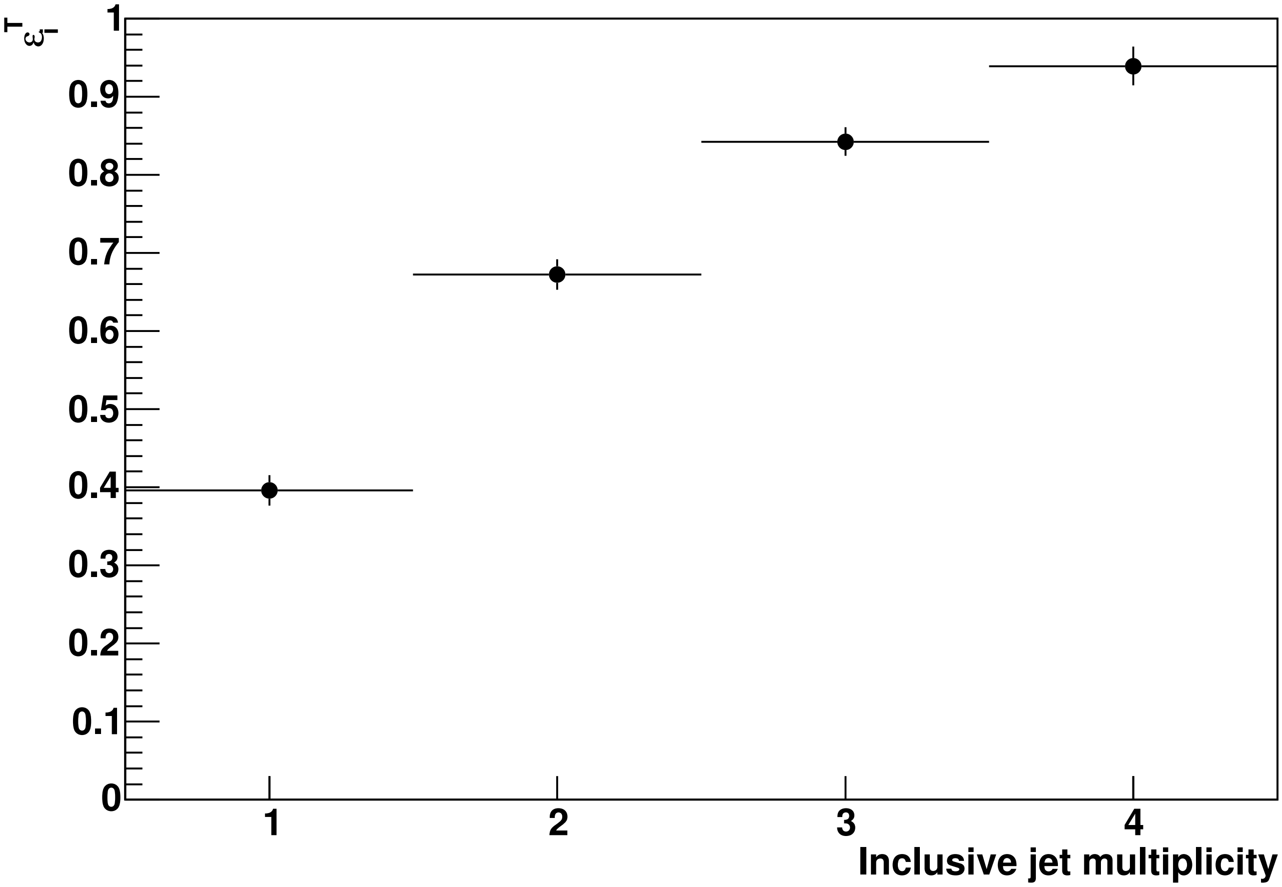

Figure 5.8: ε_i^T as a function of inclusive N_{jets} for v8-11 of the trigger.

Trigger	N_{jets}	≥ 1	≥ 2	≥ 3	≥ 4
v8-11	N_i^{obj}	5981±105	1789±60	394±29	99±12
	ε_i^T	0.40±0.02	0.66±0.02	0.84±0.02	0.94±0.02
v12	N_i^{obj}	1711±57	571 ±33	153±16	37 ±8
	ε_i^T	0.35±0.02	0.61±0.02	0.79±0.03	0.99±0.02
	$a_i^{t\bar{t}}$	0.086±0.002	0.086±0.002	0.079±0.001	0.051±0.001

Table 5.4: Summary of parameters for preselected events for triggers v8-11 and v12, used to estimate N_4^W as background to $t\bar{t}$ production.

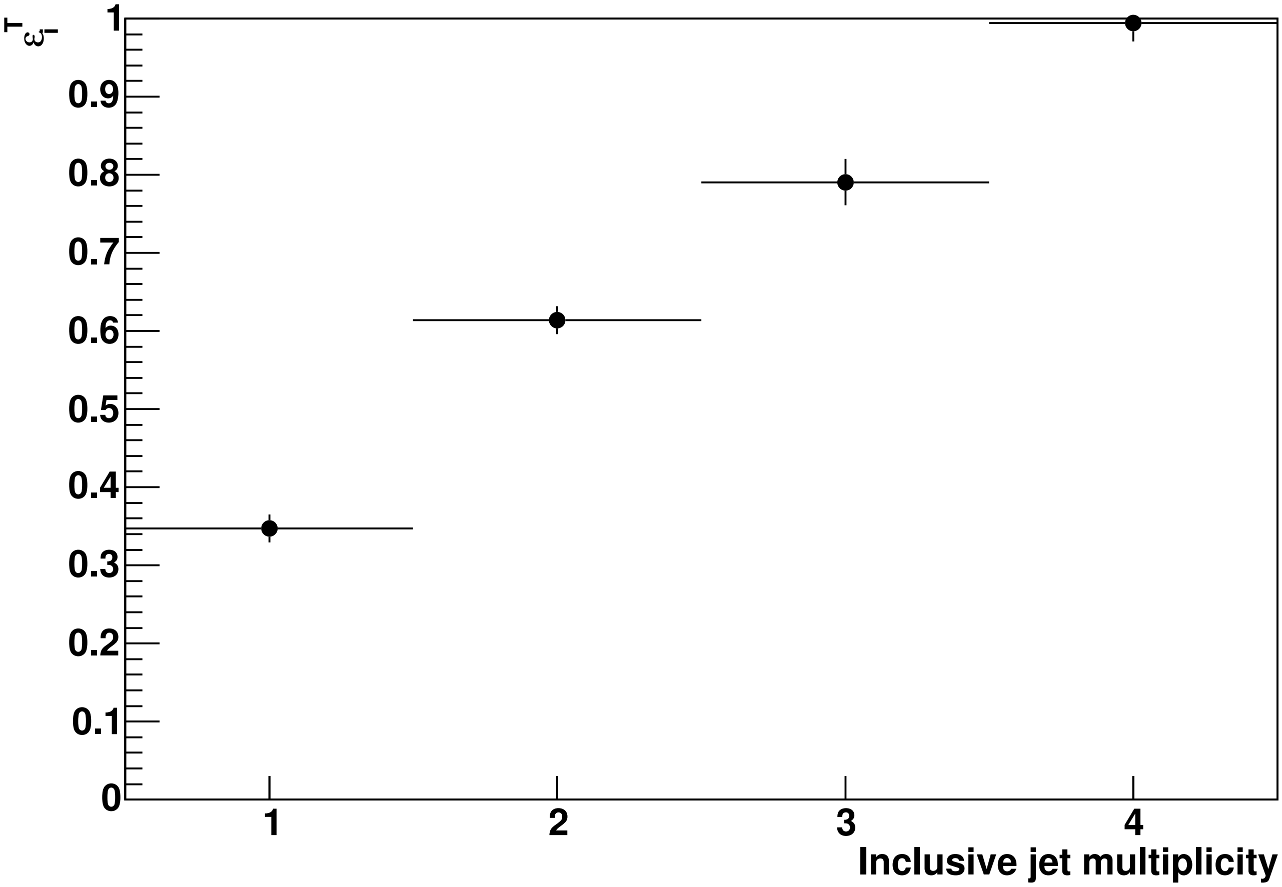

Figure 5.9: ε_i^T as a function of inclusive N_{jets} for v12 of the trigger.

Trigger	N^{obs}	N_4^W	N^{QCD}	$N_{MC}^{t\bar{t}}$
v8-11	112	66.0±10.2	12.8±3.4	19.7 ±4.4
v12	41	35.5±8.2	3.6±2.2	6.6 ±2.6
Total	153	101.5±13.1	16.4±4.0	26.3 ±5.1

Table 5.5: Summary of observed events and estimated background for v8-11 and v12 versions of the triggers obtained in the Matrix Method and Berends Scaling.

Random Grid Search

First we choose kinematic variables that are recognized to have the potential to discriminate between signal and background. One variable is the Aplanarity ($\mathcal{A}$), defined as $\frac{3}{2}$ of the smallest eigenvalue of the normalized laboratory momentum tensor ($\mathcal{M}$), where this tensor is defined by [51] :

$$\mathcal{M}_{ij} = \frac{\sum_o p_i^o p_j^o}{\sum_o |\vec{p^o}|^2} \tag{5.17}$$

where $\vec{p^o}$ is the momentum vector of a reconstructed object o, i and j are the three spatial directions in laboratory coordinates, and the objects included in the sum are the jets and the reconstructed W boson from $t \to W{+}b$ decay. This is referred to as $\mathcal{A}(W{+}\text{jets})$. Large values of $\mathcal{A}$ indicate a spherical event shape (e.g., $t\bar{t}$ events), whereas small values correspond to more planar event shapes (e.g., W+jets and multijet events). Because $t\bar{t}$ events correspond to the decay of heavy objects, whereas the jets from W+jet and multijet events contain much initial and final-state radiation [9], $\mathcal{A}$ is a good parameter for discrimination. Another topological variable is the Sphericity (S) of the event, defined as :

$$S = \frac{3}{2}(\lambda_2 + \lambda_3), \tag{5.18}$$

where λ_3 is the largest eigenvalue and λ_2 is the next largest eigenvalue of the momentum tensor in Eqs. (5.17). S is restricted to $0 \leq S \leq 1$. Typical isotropic events such as $t\bar{t}$ have large values of S. Another powerful topological variable is H_T , defined for the e+jets channels as

$$H_T = \sum_{\text{jets}} E_T \tag{5.19}$$

where the sum is over all jets with $E_T > 15$ GeV and $|\eta| <2.5$.

Events from $t\bar{t}$ production tend to have much higher values of H_T than backgrounds because E_T values of jets in $t\bar{t}$ events are typically much larger due to their origin from the decay of heavy objects.

Figures 5.10 – 5.12 show the data and background expectations for each of the topological variables. The topological variables were studied in pairs, with different combinations for achieving optimal cutoffs. Comparison of different combinations shows that $\mathcal{A}$ and H_T provide the best signal to background ratio for a given signal efficiency, and also good agreement with data and background estimation, as shown in Figs. 5.10 – 5.12.

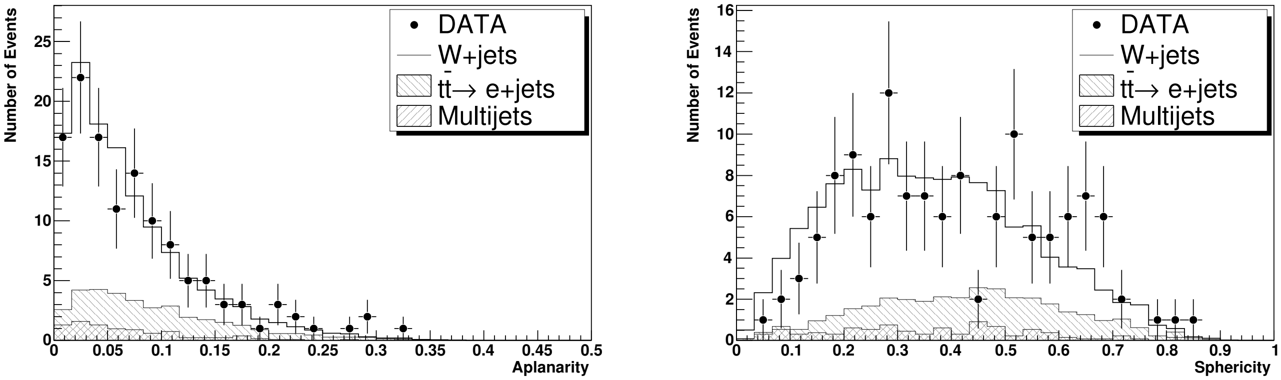

Figure 5.10: Distributions in Aplanarity and Sphericity for data (points with error bars), and fitted contributions from $t\bar{t}$, W+jets and multijet production.

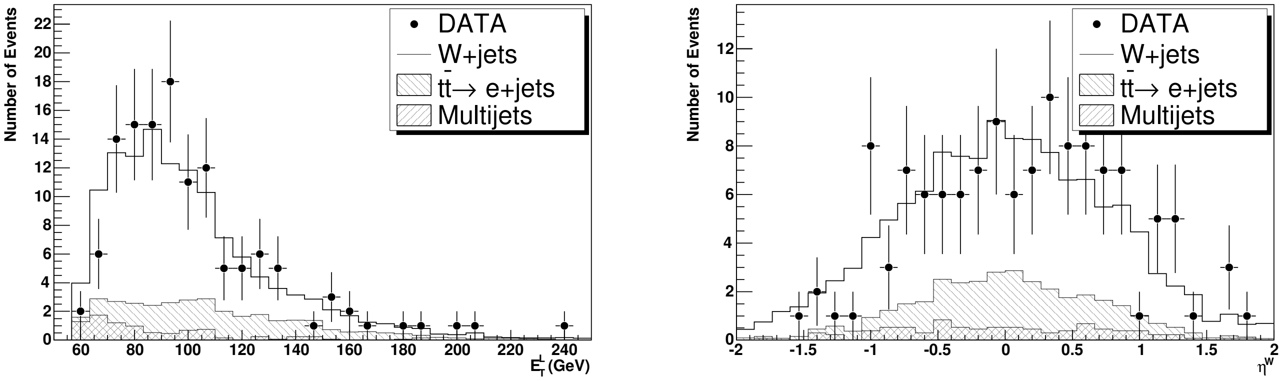

Figure 5.11: Distributions in E_T^L and η^W for data (points with error bars), and fitted contributions from $t\bar{t}$, W+jets and multijet production.

We use a Random Grid Search (RGS) method to find the values of topological variables that provide the best separation between signal and background [46]. This can improve the precision in the measurement of the $t\bar{t}$ production cross section.

The best RGS point (values of parameters to use to select events to determine

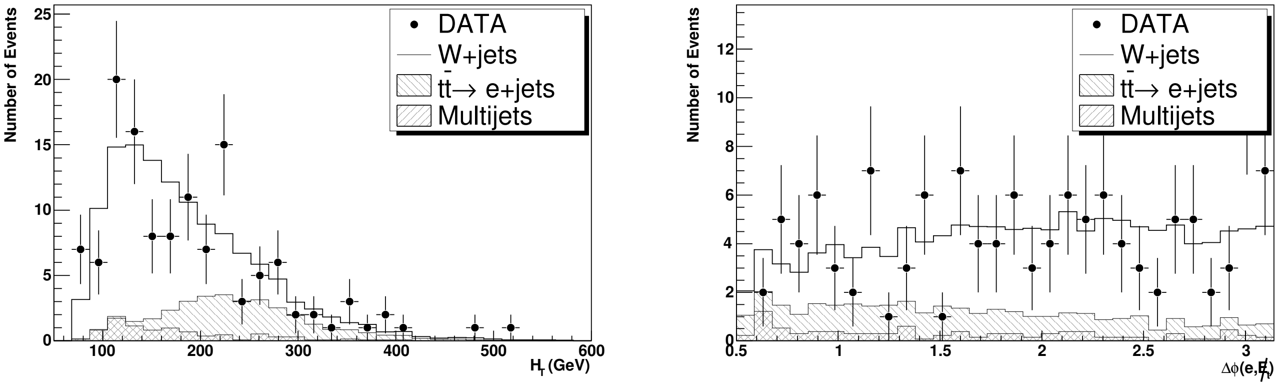

Figure 5.12: Distributions in H_T and $\Delta\phi(e, \not\!\!E_T)$ for data (points with error bars), and fitted contributions from $t\bar{t}$, W+jets and multijet production.

the $t\bar{t}$ cross section) is defined by the contour of constant uncertainty on the measured cross section ($\delta\sigma/\sigma$) that yields the most precise value of the extracted $t\bar{t}$ cross section, which is given by :

$$\sigma = \frac{N_S}{\varepsilon \cdot \mathcal{L}} = \frac{N - N_B}{\varepsilon \cdot \mathcal{L}} \tag{5.20}$$

where N, N_S and N_B are the number of observed, expected signal and expected background events, respectively, ε is the efficiency for signal (including the branching fraction of $W \to e\nu$), and $\mathcal{L}$ is the integrated luminosity. The optimal point with the smallest $\delta\sigma/\sigma$ is defined by $A > 0.017$ and $H_T > 189$ GeV (see Fig. 5.13)

After applying all selections on η^W, E_T^L, $\mathcal{A}$, and H_T, the expected background can be estimated by using a survival probability f_i for each background channel i:

$$N^{bkg} = N^{QCD}_{e+4j} \cdot f_{QCD} + N^{W}_{e+4j} \cdot f_W \tag{5.21}$$

where N^{QCD}_{e+4j} and N^{W}_{e+4j} refer, respectively, to multijet and W+jet background events in the e+jets > 3 jet selection, and f_{QCD} and f_W are the survival probability factors for the final RGS selections. There are 9 muon-tagged events and 16 secondary-vertex-tagged events in the final sample (see Table 5.6). Before RGS selection, there are 10(24) events tagged by soft muon (via secondary vertex). The RGS method therefore appears to favor selecting $t\bar{t}$ events, since the tagged events have a higher probability of being $t\bar{t}$ events [52, 53]. There is a final total of 21.5 ± 6.6 $t\bar{t}$ events found in the data.

The extracted $t\bar{t}$ cross section from our analyses is given in Chapter 6.

	N^{obs}	N^{bkg}	N^{W}	N^{QCD}	$N^{TOP(MC)}$
Preselection	153	117.9	101.5	16.4	26.3
$\lvert\eta^W\rvert < 2.0$	146	113.1	97.3	15.8	25.9
$\lvert E^L_T\rvert > 60.0$ GeV	126(10/24)	101.6	92.7	8.9	25.3
$\mathcal{A} > 0.017$	109	84.9	77.4	7.5	24.0
$H_T > 189$ GeV	46(9/16)	24.5±4.8	22.3±4.6	2.2±1.5	20.3±2.9

Table 5.6: Number of observed events and estimated background in the RGS analysis, after each of the topological selections in the e+jets channel with 4 or more jets. $N^{TOP(MC)}$ is the estimated number of $t\bar{t}$ events from Monte Carlo for σ = 7.0 pb [22, 59]. The number of muon tagged events and secondary-vertex-tagged events in the sample are given within the parentheses.

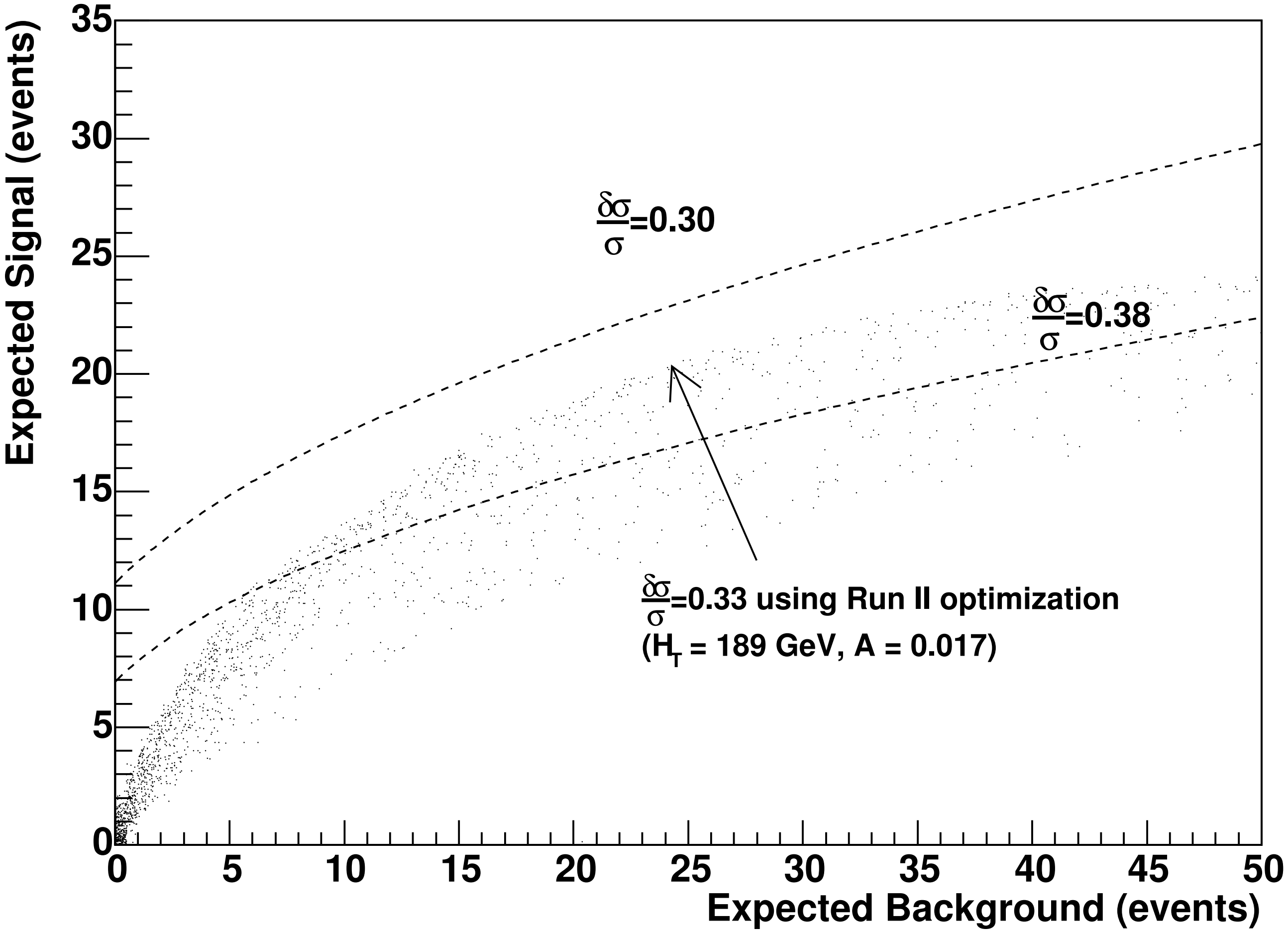

Figure 5.13: Each dot represents the expected signal vs expected background for different cutoffs in the $\mathcal{A}$ and H_T variables. The dashed curves are examples of contours of constant uncertainty on the $t\bar{t}$ cross section ($\delta\sigma/\sigma$). The arrow indicates the point that corresponds to the smallest relative uncertainty expected for the data sample.

5.2.2 Neural Network Analysis

In the previous section, we described how we estimated the $t\bar{t}$ cross section using a Random Grid Search. Although this method was used at DØ in the Run I analysis, it relies on a phenomenological assumption of Berends Scaling. Another issue is the dependence of the result on choice of variables used in the analysis and the correlation among these variables. Because no single kinematic variable has sufficient sensitivity to discriminate between signal and background, correlations among kinematic variables must be considered, and using Neural Networks (NN) is one way to do this. In principle, this can enhance the significance of $t\bar{t}$ signal. An advantage of Neural Networks is that the background estimation is independent of Berends Scaling because we can estimate the fraction of background directly by using signal and background samples in constructing the Neural Network, and then comparing the output to data.

In our analysis, we use the TFractionFitter class in the ROOT package [54] to estimate signal and background fractions from the application of the results from Neural Networks to data. This procedure estimates the fractions of different events through a fit to the NN output in data [55], and takes account of statistical uncertainties in both data and any Monte Carlo through a standard likelihood fit using Poisson statistics [56].

In our analysis, the Neural Network is trained using a $t\bar{t}$ Monte Carlo sample for signal and a sample of W+jets Monte Carlo events for background. We determine the response of this NN to multijet data, but, in the final fit to the data, we use the fraction of multijet background that is estimated from the Matrix Method, combined with the W+jets contribution to represent the full background. It would have been better to use multijet background as a separate contribution to the NN, but the multijet fraction is very small, and the analysis would not have been sensitive to it. When there is more data, the multijet fraction can be used as an independent parameter, so that the estimate of background is independent of the Matrix Method, which can provide a good cross check.

We used the following kinematic variables for training our Neural Network :

- As discussed in Section 5.2.1, W+jets and multijet events are less likely to be spherical, because they contain gluon radiation, while $t\bar{t}$ events reflect the large mass of the top quark. Thus the Aplanarity $\mathcal{A}$ for $t\bar{t}$ events is larger than that for W+jets or multijet production [51].

- Sphericity effectively reflects a sum over p_T^2 relative to the event axis, and an isotropic event corresponds to $S \approx 1$. Hence, as argued before, $t\bar{t}$ events are expected to be more isotropic than W+jets and multijet events, because of the presence of extra gluon radiation in the background processes.

- H'_{T2} is defined as H_{T2}/H_z, which provides a measure of the "centrality" of events. H_{T2} is defined by the scalar sum of the p_T of just the jets (H_T), but excluding the leading jet, and H_z is the scalar sum of the $|p_z|$ of the jets, the lepton and neutrino. This variable was found to give an effective discrimination between signal and background in top-mass analyses in Run I [57].

- K'_{Tmin} is defined as $\Delta R_{jj}^{min} \cdot (E_T^{min}/E_T^W)$, and provides a measure of the minimum relative p_T among jets. This variable was also used in the top-mass analyses in Run I [57]. ΔR_{jj}^{min} is the minimum separation in $\eta - \phi$ space between any pair of jets, and E_T^{min} is the E_T of the lesser jet of that pair. $E_T^W = E_T^{lepton} + \not\!\!E_T$ is introduced to reduce the correlation of this variable with jet energy (and the mass of the top quark). Only the four leading jets in an event are used to define this variable.

- $\Delta\phi(e, \not\!\!E_T)$ is used because the electron and neutrino are decay products of a W boson in both $t\bar{t}$ events and in W+jets production. These $\Delta\phi(e, \not\!\!E_T)$ tend to be relatively uniformly distributed (depending on the boost of the W boson), but, for multijet events, the $\Delta\phi(e, \not\!\!E_T)$ spectrum peaks around 0 because $\not\!\!E_T$ is often caused by a downward fluctuation in the measurement of the energy of the jet that mimics an electron.

- eH_T is the scalar sum of electron p_T and jet H_T. Because of the large mass of the top quark and the requirement that one W boson decays to two jets, a larger fraction of the transverse energy is carried away by jets in $t\bar{t}$ events than in W+jets or multijet background.

Figures 5.14 – 5.16 provide a comparison of distributions in the above variables for $t\bar{t}$ signal and W+jets Monte Carlo events. We see that they all offer some discrimination between signal and background.

Using the above kinematic variables, we trained a Neural Network using $t\bar{t}$ and W+ jets MC samples, and Fig. 5.17 shows plots that examine the performance of the Neural Network. Figure 5.18 shows the response of the NN to $t\bar{t}$ and W+jets samples – different from those used to train the NN and Fig. 5.19 displays the qualitative structure of the NN. Figures 5.20 and 5.21 show the distribution of the NN output for the $t\bar{t}$ candidate events (points with error bars). Figure 5.20 gives the result of a fit to the output of the $t\bar{t}$ and combined W+ jets and multijet background, using the TFractionFitter. The solid darker line corresponds to the total fit, which is not the same as a simple weighted sum of the input distributions because the fit takes account of statistical uncertainties in both data and Monte Carlo. Figure 5.21 shows the final results of Fig. 5.20, but indicates the specific contributions of the tagged events in the data sample. As in RGS analysis, these favor $t\bar{t}$ signal. Table 5.7 tabulates the results. Comparing this with the RGS method in Table 5.6, the two results show good agreement, and support the validity of the Berends Scaling hypothesis. The $t\bar{t}$ cross section from this analysis is also given in Chapter 6.

N^{obs}	$N^{t\bar{t}}$	N^{W}	N^{QCD}	$\mathcal{L}$	$t\bar{t}$ fraction
126	28.3±10.7	88.2±15.4	9.4±4.1	165.9	0.225 ± 0.085

Table 5.7: Summary of the fitted values from TFraction Fitter using the Neural Network method.

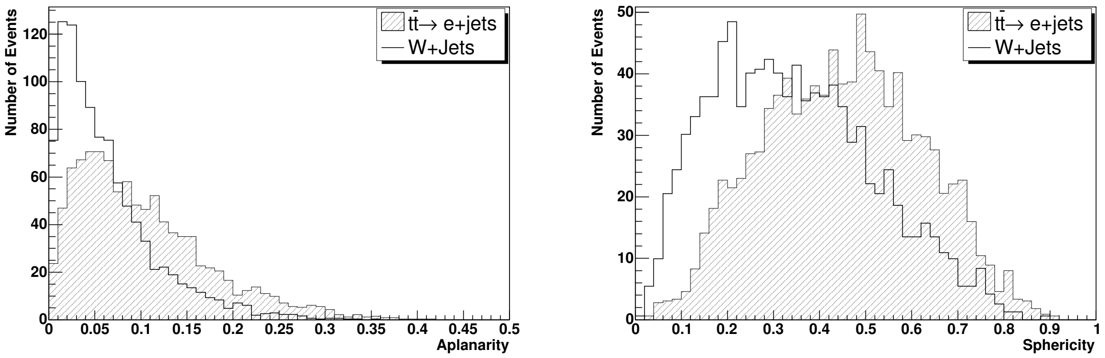

Figure 5.14: Distributions in $\mathcal{A}$ and S for $t\bar{t}$ and W+jets .

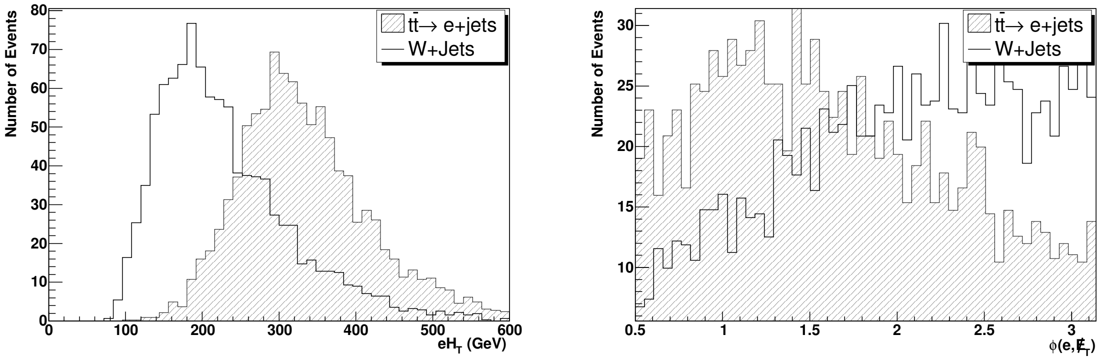

Figure 5.15: Distributions in eH_T and $\phi(e, \not{E}_T)$ for $t\bar{t}$ and W+jets .

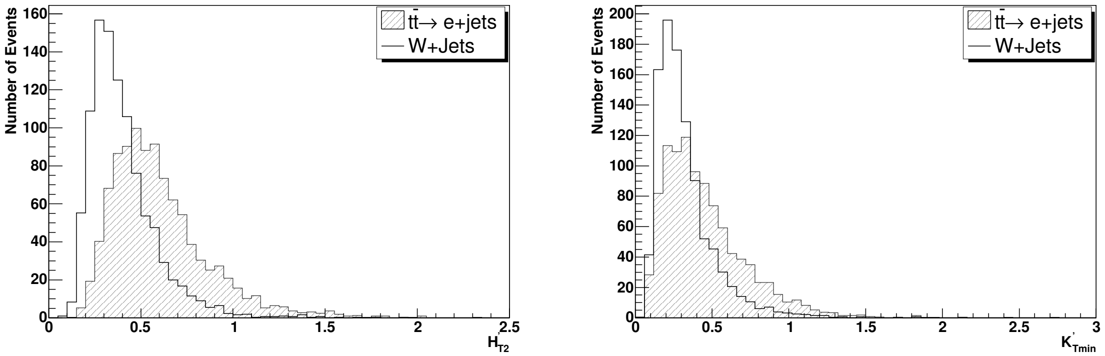

Figure 5.16: Distributions in H'_{T2} and K'_{Tmin} for $t\bar{t}$ and W+jets .

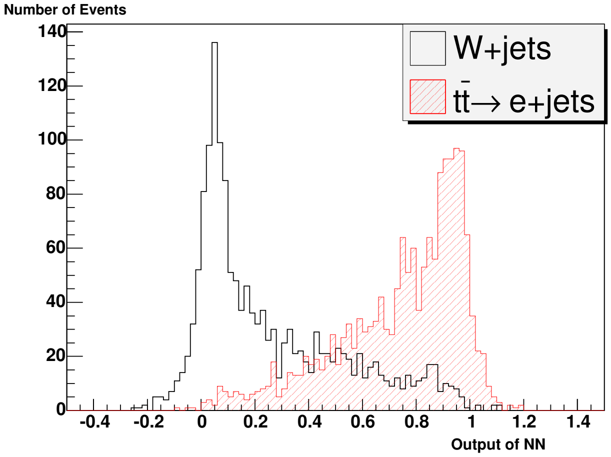

Figure 5.17: The output of the Neural Network on training samples of $t\bar{t}$ and $W+$ jets events.

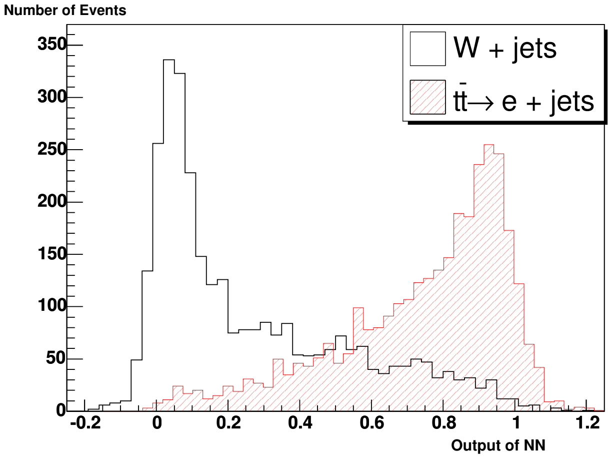

Figure 5.18: The output of the Neural Network on test samples of $t\bar{t}$ and $W+$ jets events.

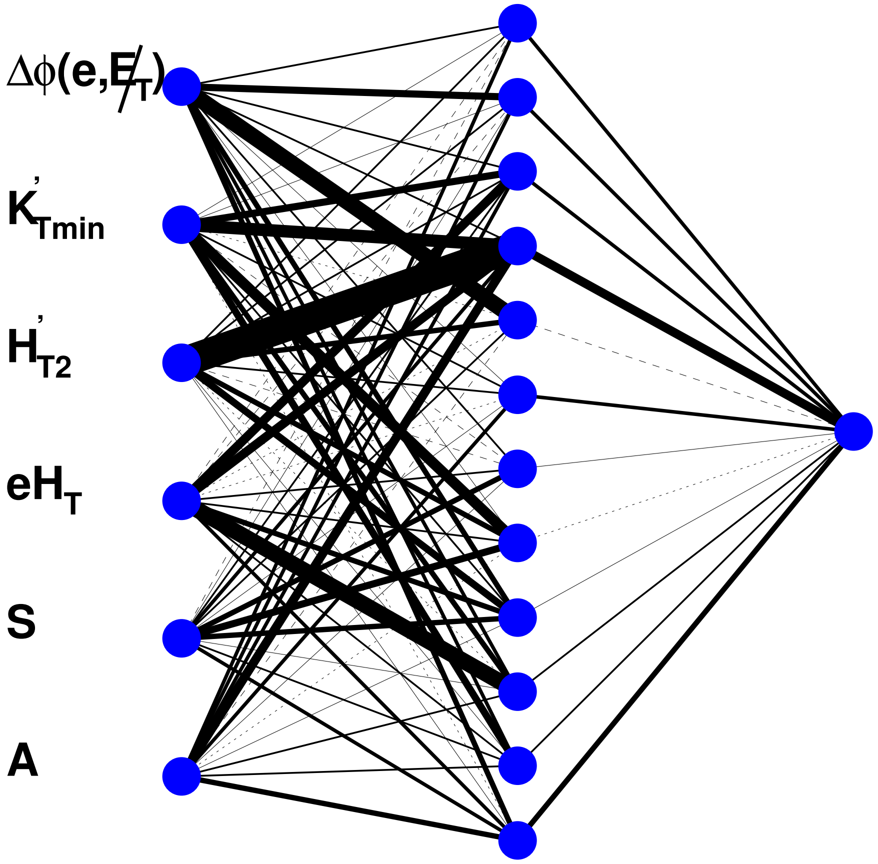

Figure 5.19: Structure of the Neural Network used for extracting $t\bar{t}$ signal (six input nodes, twelve hidden nodes, and one output node). Neurons are depicted by a disks, and synapses by lines connecting neurons. The line width is proportional to the impact of the contribution to the final decision.

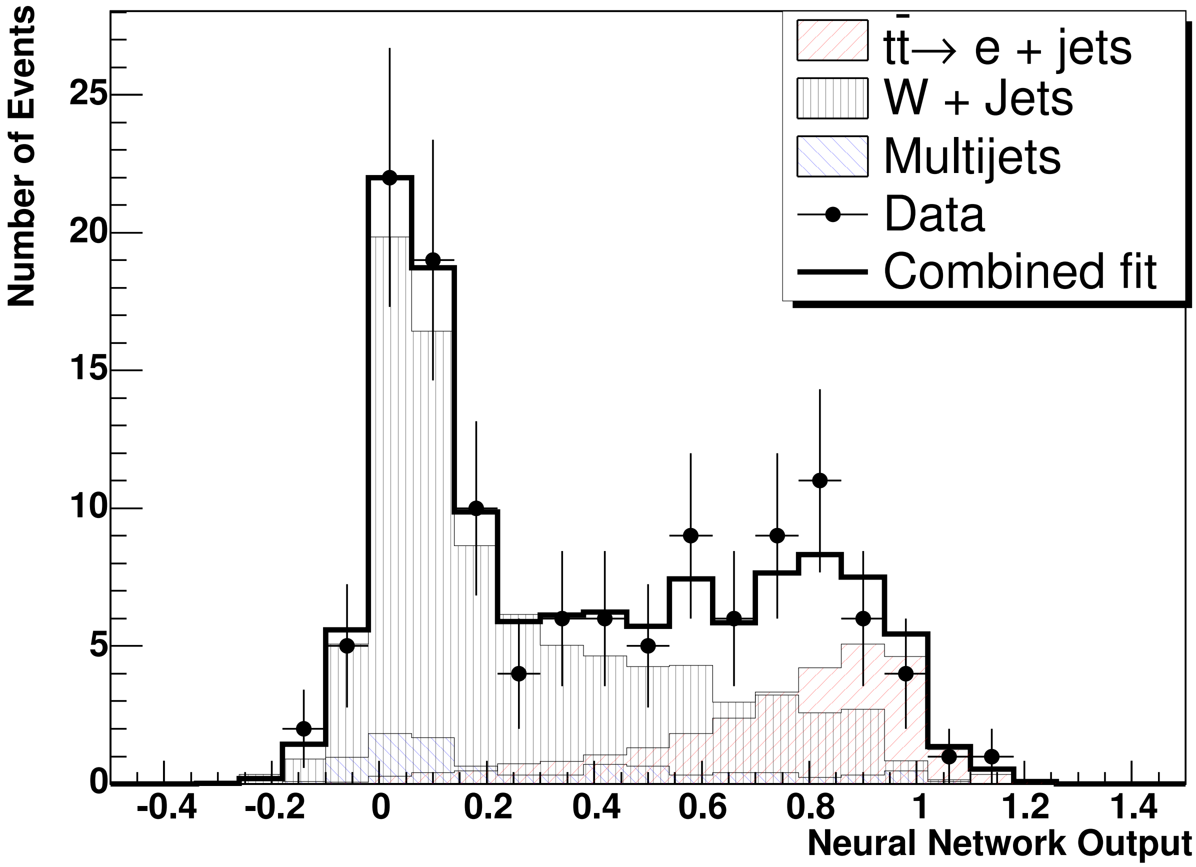

Figure 5.20: Results of a fit of e+jets data to signal and background contributions using the TFractionFitter. The thick solid line is the histogram corresponding to the total fit (which is not the same as a simple weighted sum of the separate components).

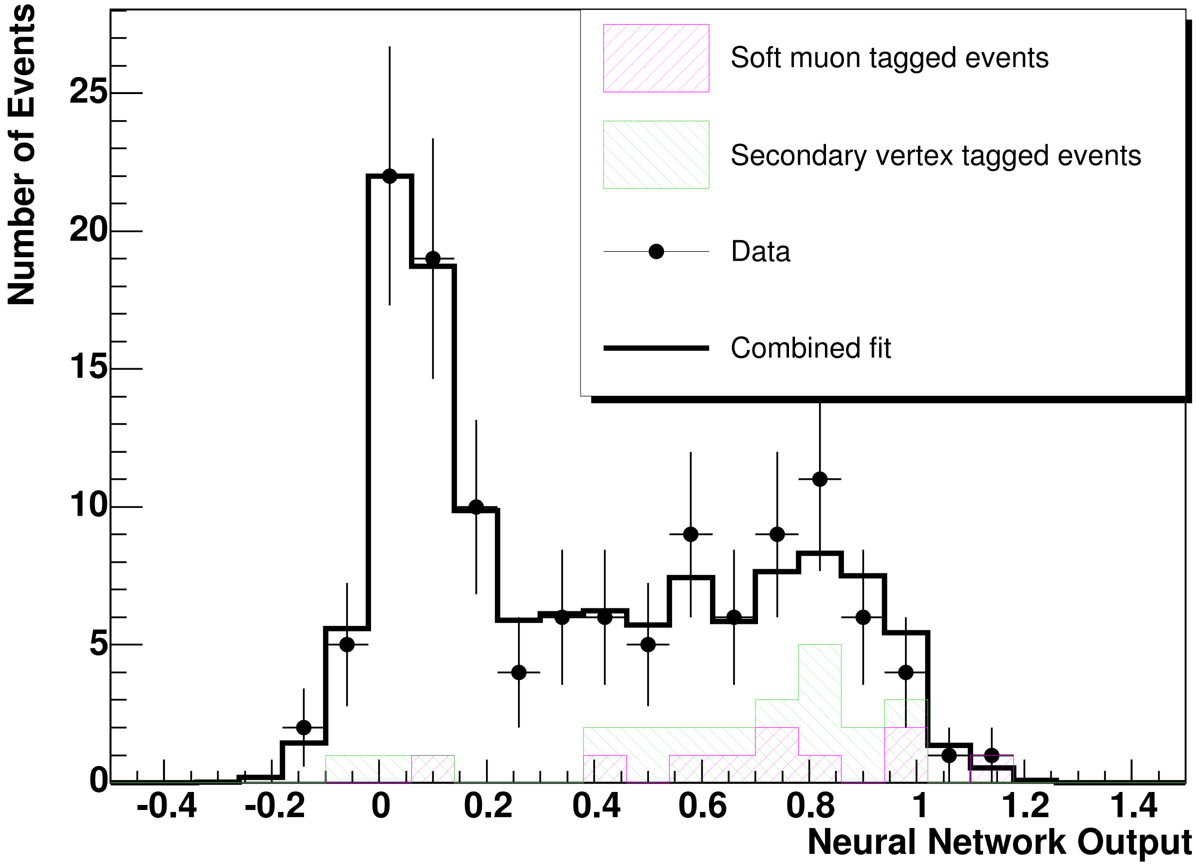

Figure 5.21: Same as Fig. 5.20, but showing contributions from soft-muon tagged events and secondary-vertex tagged events.

5.3 Selection Efficiencies

As indicated previously, the efficiencies for electron selections are obtained using $Z \rightarrow e^+e^-$ data, and a correction factor (CF) applied for topological differences between $Z \rightarrow e^+e^-$ and $t\bar{t}$ events, derived from a comparison of $Z \rightarrow e^+e^-$ and $t\bar{t}$ Monte Carlo samples:

$$\varepsilon_{t\bar{t}}^{data} = \varepsilon_{Ze^+e^-}^{data} \cdot \frac{\varepsilon_{t\bar{t}}^{MC}}{\varepsilon_{Ze^+e^-}^{MC}}(CF) \tag{5.22}$$

Selection	$\varepsilon_{t\bar{t}}^{MC}$	$\varepsilon_{Ze^+e^-}^{MC}$	CF
electron ID	0.833 ± 0.003	0.966± 0.0003	0.862± 0.003
electron loose selection	0.855 ± 0.003	0.952± 0.0005	0.898± 0.003
electron tight selection	0.849 ± 0.003	0.937± 0.0005	0.906± 0.003
Total CF	(including reconstruction)		0.703± 0.005

Table 5.8: Total corrections for electrons. The final efficiency of 0.703± 0.005 ignores any small energy dependence.

All other efficiencies are determined from $t\bar{t}$ Monte Carlo, generated with the ALPGEN generator for a top mass of 175 GeV/c^2. Any sensitivity to the top mass is taken as a systematic uncertainty. The inclusive $t\bar{t} \rightarrow$ lepton+jets sample is used for determining total efficiencies in order to account for possible contributions to the signal from $t\bar{t} \rightarrow \tau$+jets $\rightarrow e$+jets. The efficiencies of all preselections are summarized in Table 5.9.

Selection	Efficiency
electron Acceptance$\cdot\mathcal{B}r$	0.136 ± 0.001
CF for electron reconstruction	0.984 ± 0.004
electron ID	0.917 ± 0.007
electron loose selection	0.903 ± 0.006
electron tight selection	0.815 ± 0.009
CF for electrons	0.703 ± 0.005
$E_T(e) > 20$ GeV	0.921 ± 0.003
$\lvert\eta^e\rvert < 1.1$	0.916 ± 0.004
Primary Vertex	0.989 ± 0.008
$\lvert PV(e) - PV\rvert < 1.0$ cm	0.964 ± 0.001
$\not{E}_T > 20$ GeV	0.899 ± 0.003
$\Delta\phi(e, \not{E}_T) > 0.5$	0.858 ± 0.004
Njets ≥ 4	0.588 ± 0.006
Trigger efficiency	0.932 ± 0.029
Total Signal Efficiency$\cdot\mathcal{B}r$	0.021 ± 0.001

Table 5.9: Total event efficiency from all selections, including branching fractions ($\mathcal{B}r$) of $t\bar{t}$ into the e+jets channels. The final efficiency corresponds to the product of the individual contributions.

5.4 Systematic Uncertainties

Systematic uncertainties contribute in a major way to the total uncertainty on the measurement of the $t\bar{t}$ cross section. The main sources arise from uncertainties in:

Primary Vertex: This uncertainty is taken from the statistical uncertainty on the efficiency measured in the preselected sample, without applying the tight electron selection and the Δz criteria on the electron [47].

Δz(PV(e)-PV): This is defined as the uncertainty in the efficiency from the Δz requirement [47].

EM Reconstruction: This uncertainty is determined from the dependence of the measured reconstruction efficiency in $Z \rightarrow e^+e^-$ data on variations in the Z mass window [22].

EM Identification: This corresponds to the systematic uncertainty on the measurements using $Z \rightarrow e^+e^-$ data, which arise from the uncertainty in the estimation of the background [22].

EM Tracking: This uncertainty arises from the systematic uncertainty on the measurements in $Z \rightarrow e^+e^-$ data, due to the uncertainty in background estimation [22].

EM Tight Selection: This uncertainty is determined from the systematic uncertainty on the measurement in $Z \to e^+e^-$ data, and arises from the uncertainty in background estimation.

Jet Energy Resolution (JER): This uncertainty is obtained by varying the JER by one standard deviation (s.d.) and redetermining the efficiency.

Jet Energy Scale (JES): This uncertainty determined by varying the JES by one s.d., where the s.d. can be written:

$$\sigma = \sqrt{\sigma^2_{stat,data} + \sigma^2_{syst,data} + \sigma^2_{stat,MC} + \sigma^2_{syst,MC}} \tag{5.23}$$

and then redetermining the selection efficiency.

Jet Reconstruction and Identification: The difference in jet reconstruction and identification efficiency between data and Monte Carlo requires a correction factor defined by dividing the combined jet reconstruction and identification efficiency measured in data and the efficiency measured in Monte Carlo. The efficiencies and scale factor are measured using γ+jet events [47].

Top Mass: This uncertainty is determined from the difference in efficiencies for a top mass of m_t = 170 GeV/c^2 and m_t = 180 GeV/c^2, instead of m_t = 175 GeV GeV/c^2.

Trigger Efficiency: The uncertainty on the number of selected $t\bar{t}$ signal events due to the systematic uncertainty on the trigger efficiency is obtained by varying the parametrization of the efficiency by one s.d.

Statistical uncertainty: This uncertainty is determined from the available Monte Carlo statistics.

Uncertainty on ε_{sig}: The uncertainty on ε_{sig} is propagated to the uncertainty on the estimated signal.

Uncertainty on ε_{QCD}: The uncertainty on ε_{QCD} is propagated to the uncertainty on the estimated signal.

Source	$\Delta\varepsilon$(%)	RGS (%)	NN(%)
Primary Vertex	± 1		
Δz(PV(e)-PV)	± 1		
EM Reconstruction	± 1.5		
EM Identification	± 0.1		
EM Tracking	± 0.4		
EM Tight Selection	± 0.5		
Jet Energy Resolution	$^{+1.1}_{-1.0}$	$^{+7.5}_{-2.6}$	$^{+0.4}_{-11.3}$
Jet Energy Scale	$^{+4.4}_{-8.4}$	$^{+12.9}_{-4.0}$	$^{+9.0}_{-1.6}$
Jet Reconstruction and Identification	± 9.6	± 2.4	± 3.4
Top mass	± 2		
L1 electron trigger	$^{+2.09}_{-2.92}$		
L2 electron trigger	~ 0		
L3 electron trigger	± 0.9		
L1 Jet trigger	$^{+0.02}_{-0.05}$		
L2 Jet trigger	~ 0		
L3 Jet trigger	$^{+0.03}_{-0.05}$		
MC Statistical uncertainty	± 4		
Uncertainty on ε_{sig}	± 1		
Uncertainty on ε_{QCD}	± 1		
Berends Scaling		± 3.9	
Total systematic Uncertainty for NN			± 7.7

Table 5.10: Summary of relative systematic uncertainties on the $t\bar{t}$ cross section, where ± reflects the effect of a change by one s.d. in that source.

Chapter 6

Results & Conclusion

The cross section σ for $t\bar{t}$ production is calculated from:

$$\sigma = \frac{N_{obs} - N_{bkg}}{\mathcal{B} \cdot \mathcal{L} \cdot \varepsilon} \tag{6.1}$$

where N_{obs}, N_{bkg}, $\mathcal{B}$, $\mathcal{L}$ and ε are, respectively, the number of observed events, the number of background events, the branching fraction for $t\bar{t} \rightarrow e$+jets, the integrated luminosity and the total selection efficiency.

The cross section for the RGS method is estimated using maximum likelihood method, assuming Poisson statistics for the small number of observed events [58]. The likelihood L is defined as the Poisson probability for obtaining the expected number of events $\hat{N}$:

$$\hat{N} = \sigma \cdot \mathcal{B} \cdot \mathcal{L} \cdot \varepsilon + N_{bkg} \tag{6.2}$$

$$\mathsf{L}(\sigma, N_{obs}, N_{bkg}, \mathcal{B}, \mathcal{L}, \varepsilon) = \frac{\hat{N}^{N_{obs}}}{N_{obs}!} e^{-\hat{N}} \tag{6.3}$$

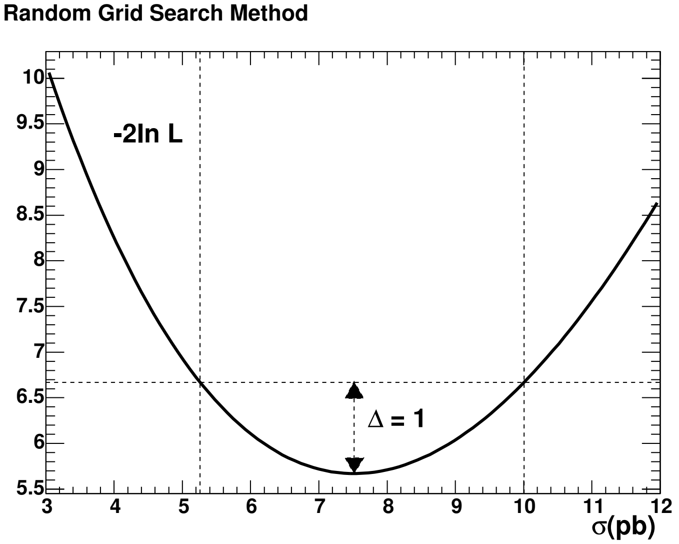

Figure 6.1: –2ln L as a function of σ for the RGS.

Figures 6.1 shows -2ln L as a function of σ, using the results of RGS. The estimated cross section is defined by the minimum in –2ln L. Assuming a Gaussian probability distribution, the statistical uncertainty is determined from the width of the parabolic curve at the minimum: $\pm\delta\sigma$ corresponds to the change in σ when

-2ln L changes by one unit relative to the minimum.

The cross section for the NN method is extracted using Eq.(6.1), and the statistical uncertainty is estimated directly from the fitting error by TFractionFitter. The fitting error is 38% as shown in Table 5.7, because the $t\bar{t}$ fraction of events in the tight selection provides only a small contribution to the fit. For the W+jets fraction, the result is 0.78±0.13, which has a 17% statistical uncertainty. Improving the $t\bar{t}$ purity through more restrictive selections would provide smaller uncertainties in the fit, but this cannot be done until the experiment accumulates more data.

The values of the $t\bar{t}$ cross sections estimated from the e+jets channel are:

$$\begin{aligned} \text{RGS} &: \quad \sigma_{p\overline{p}\to t\bar{t}+X} = 7.9^{+2.6}_{-2.4}\,(\text{stat})\,^{+2.2}_{-2.3}\,(\text{syst})\;\pm 0.5\,(\mathcal{L})\text{ pb;} \\ \text{NN} &: \quad \sigma_{p\overline{p}\to t\bar{t}+X} = 8.1^{+3.1}_{-3.1}\,(\text{stat})\,^{+1.8}_{-1.3}\,(\text{syst})\;\pm 0.5\,(\mathcal{L})\text{ pb.} \end{aligned}$$

where the errors correspond to statistical, other systematics, and the uncertainty in luminosity.

Our measurements are consistent within error with the value expected from the Standard Model ($\sigma_{p\overline{p}\to t\bar{t}+X} = 6.77 \pm 0.42$ pb at $\sqrt{s} = 1.96$ TeV) [59]. The largest systematic uncertainty is from JES, which is estimated to be about 15% for RGS and 10% for NN. This uncertainty arises from jet measurements and the use of variables such as "H_T" (sums in jet p_T). By improving the JES uncertainty by a factor of two, the systematic uncertainty whould drop to 10% for RGS and 5% for NN. This will be possible when there is sufficient data to normalize the JES to $W \rightarrow 2$ jet decays in these events. Other improvements from higher luminosity, particle identification, and techniques for discrimination of backgrounds should also be feasible. When this is carried out, we expect $\sigma_{t\bar{t}}$ to provide a better test of the SM, but because of the ≈ 6 % uncertainty in the theoretical model, this will remain only a qualitative test of the Standard Model at the 10% level of accuracy. (The uncertainty on $\mathcal{L}$ is likely to be reduced by at least a factor of 2 when the data can be normalized to the W+jets production cross section, which has less theoretical ambiguity.)

Bibliography

[1] F. Abe et al., Phys. Rev. Lett., **74**, 2626 (1995).

[2] S. Abachi et al., Phys. Rev. Lett., **74**, 2632 (1995).

[3] The DØ collaboration, Nature, **429**, 638 (2004).

[4] V. M. Abazov et al., Phys. Rev., **D67**, 012004 (2003).

[5] C. Quigg, arXiv:hep-ph/0001145 (1995).

[6] M. Perl et al., Phys. Rev. Lett., **35**, 1489 (1975).

[7] S. W. Herb et al., Phys. Rev. Lett., **39**, 252 (1977).

[8] Campagnari, Claudio and Franklin, Melissa, Rev. Mod. Phys., **69**, 137 (1997).

[9] P. Bhat et al., Int. J. Mod. Phys., **A13**, 5113 (1998).

[10] S. Eidelman et al. [Particle Data Group Collaboration], Phys. Lett. B **592**, 1 (2004).

[11] A. K. Das and T. Ferbel, "Introduction to nuclear and particle physics", World Scientific (2003).

[12] J. Womersley et al., Eur. Phys. J., **C4S1**, 12 (2002).

[13] R. Moore, FERMILAB-CONF-02-320-E (2002).

[14] J. Ellison et al., FERMILAB-CONF-01-012-E (2001).

[15] Run II Handbook, http://www-bd.fnal.gov/lug/runII_handbook/RunII_index.html.

[16] S. Abachi et al., FERMILAB-PUB-96-357-E (1996).

[17] S. Abachi et al., Nucl. Instrum. Meth., **A338**, 185(1994).

[18] L. Groer et al., FERMILAB-CONF-00-322-E (2001).

[19] S. Ahn et al., DØ Note 3973 (2002).

[20] C. Miao et al., FERMILAB-CONF-98-395-E (1998).

[21] G. Blazey et al., FERMILAB-CONF-97-395-E (1997).

[22] Top Physics Physics Group, DØ Note 4419 (2004).

[23] M. Angelou et al., DØ Note 4512, (2004).

[24] RECO Status, http://www-d0.fnal.gov/computing/algorithms/status/index.html.

[25] DØOM, http://www-d0.fnal.gov/computing/infrastructure/d0om/d0om.html.

[26] Serban Protopopescu, Stephanie Baffioni, Elemer Nagy, DØ Note 3979 (2002).

[27] What is SAM ?, http://projects.fnal.gov/samgrid/WhatisSAM.html.

[28] Lee Lueking et al., FERMILAB-CONF-97-070-E (1997).

[29] Common Sample Group, http://www-d0.fnal.gov/Run2Physics/cs/index.html.

[30] top_dq package, http://www-d0.fnal.gov/Run2Physics/top/index.html.

[31] M. Mangano, et al., JHEP, **07**, 001 (2003).

[32] PYTHIA, http://www.thep.lu.se/tf2/staff/torbjorn/Pythia.html.

[33] Generators, http://www-d0.fnal.gov/computing/MonteCarlo/MonteCarlo.html.

[34] DØGSTAR, http://www-d0.fnal.gov/computing/MonteCarlo/simulation/d0gstar.html.

[35] R. Brun and F. Carminati, *9th International Conference on Computing in High-energy Physics (CHEP 91)*, Tsukuba, Japan (1991).

[36] DØSIM, http://www-d0.fnal.gov/computing/MonteCarlo/simulation/d0sim.html

[37] J. Kozminski et al., DØ Note 4449 (2004).

[38] MLPFIT package, http://schwind.home.cern.ch/schwind/MLPfit.html

[39] S. Tentindo-Repond, H. B. Prosper and P. C. Bhat, *7th International Workshop on Advanced Computing and Analysis Techniques in Physics Research (ACAT 2000)*, Batavia, Illinois (2000).

[40] J. Zhu V. Buescher. DØ Note 4171 (2003).

[41] M. Zielinski et al., DØ Note 3535 (1998).

[42] G. Blazey et al., DØNte 3750 (2000)

[43] JETID v5.0, http://www-d0.fnal.gov/computing/algorithms/calgo/jet/jetID_p14.html.

[44] B. Knuteson, M. Strovink, B. Olivier, U. Bassler, F. Fleuret, G. Bernardi, DØ Note 3629 (1999).

[45] A. Garcia-Bellido et al., DØ Note 4320 (2004).

[46] N. Amos, C. Stewart, P. Bhat, C. Cretsinger, E. Won, W. Dharmaratna and H. B. Prosper, *International Conference on Computing in High-energy Physics (CHEP 95)*, Rio de Janeiro, Brazil (1995).

[47] Top Physics Group, Measurement of the $t\bar{t}$ production cross section at $\sqrt{s} =$ 1.96 TeV in the lepton + jets final states using a topological method (2004) unpublished.

[48] F. Berends et al., Nucl. Phys., **B357**, 32 (1991).

[49] Top Physics Group, DØ Note 4116 (2003).

[50] Z. Zhou, Ph.D. Thesis, Iowa State University, (2001).

[51] V. Barger and R. Phillips., Collider physics., (1938) Frontiers in Physics.

[52] F. Beaudette and J. Grivaz, DØ Note 4206 (2003).

[53] C. Clement et al., DØ Note 4626 (2004).

[54] R. Brun et al., Root, an object oriented data analysis framework. *CERN School of Computing (CSC 2000)*, Marathon, Greece (2000).

[55] R. Barlow and C. Beeston., Comp. Phys. Comm., **77**, 219 (1993).

[56] Steve Baker and Robert D. Cousins., Nucl. Instrum. Meth., **A221**, 437 (1984).

[57] B. Abbott et al., Phys. Rev., **D58**, 052001 (1998).

[58] Top Physics Group., DØ Note 4246 (2003).

[59] N. Kidonakis et al., Eur. Phys. J., **C33**, S466 (2004).